Investigating Granulars for laboratory experiments in context of tectonics and surface process

Dr. N.L. Dongre.

The San Andreas fault in California marks the meeting of the Pacific and North American tectonic plates. Earth's tectonic plates may have taken as long as 1 billion years to form..The plates — interlocking slabs of crust that float on Earth's viscous upper mantle — were created by a process similar to the subduction seen today when one plate dives below another.

Abstract

A new granular material (MatIV) developed to study experimentally landscape evolution in active mountain belt piedmonts. Its composition and related physical properties have been determined using empirical criteria derived from the scaling of deformation, erosion-transport and sedimentation natural processes. MatIV is a water-saturated composite material made up with 4 granular components (silica powder, glass microbeads, plastic powder and graphite) whose physical, mechanical and erosion-related properties were measured with different laboratory tests. Mechanical measurements were made on a modified Hubbert-type direct shear apparatus. Erosion-related properties were determined using an experimental set-up that allows quantifying the erosion/sedimentation budget from tilted relaxation topographies. For MatIV, it is also investigated the evolution of mean erosion rates and stream power erosion law exponents in 1D as a function of slope.

The results indicate that MatIV satisfies most of the defined criteria. It deforms brittlely according to the linear Mohr-Coulomb failure criterion and localizes deformation along discrete faults. Its erosion pattern is characterized by realistic hillslope and channelized processes (slope diffusion, mass wasting, channel incision). During transport, eroded particles are sorted depending on their density and shape, which results in stratified alluvial deposits displaying lateral facies variations. To evaluate the degree of similitude between model and nature, a new experimental device was used that combines accretionary wedge deformation mechanisms and surface runoff erosion processes. Results indicate that MatIV succeeded in producing detailed morphological and sedimentological features (drainage basin, channel network, terrace, syntectonic alluvial fan). Geometric, kinematic and dynamic similarity criteria have been investigated to compare precisely model to nature. Although scaling is incomplete, it yields particularly informative orders of magnitude. With all these characteristics, MatIV appears as a very promising material to investigate experimentally a wide range of scientific questions dealing with relief dynamics and interactions between tectonics, erosion and sedimentation processes.

1. Introduction

Understanding the dynamic interactions between tectonics, erosion and sedimentation in mountain belts is a difficult challenge because field morphological and structural observations correspond to a "snapshot" in the long geological history of the topography. In addition, they usually deliver sparse datasets in both time and space that are difficult to integrate into comprehensive 4D evolution models. To access to relief dynamics, experimental modeling can be used as a good complement to fieldwork investigations. Up to now, two types of approaches can be distinguished. First, the "tectonic" approach, commonly called "sandbox modeling", has been intensively used for a long time to study accretionary wedge and fold-and-thrust belt dynamics (Fig. 1a) (Cadell, 1888; Davis et al., 1983; Hubbert, 1951; Malavieille, 1984). Erosion and sedimentation are mainly modeled in 2 dimensions by respectively removing material from high topographies (Konstantinovskaia and Malavieille, 2005, 2011; Mulugeta and Koyi, 1987) and by sifting fresh material in basins (Fig. 1a) (Bonnet et al., 2007; Cobbold et al., 1993; Larroque et al., 1995; Malavieille, 2010; Malavieille and Konstantinovskaya, 2010). Second, the "geomorphic" approach is focused mainly on landscape dynamics in response to changes in tectonic, climatic or initial boundary conditions (Babault et al., 2005; Bonnet and Crave, 2003; Hasbargen and Paola, 2000; Lague et al., 2003; Pelletier, 2003; Rohais et al., 2011). Erosion and sedimentation are triggered by sprinkling water micro-droplets on the model surface whereas tectonics consists essentially in pure uplift. Model uplift is performed mechanically by lowering channel outlet to decrease the river base-level or by elevating a central column of material (Fig. 1b).

Model materials in both set-ups are generally granular media (such as sands, beads or powders) because their mechanical properties are suitable to simulate deformation and erosion of rocks in the upper continental crust (Hubbert, 1951; Lohrmann et al., 2003; Ramberg, 1981). In tectonic modeling, materials are mainly dry quartz sand or silts (Cobbold and Castro, 1999), but other components are also used to weaken or strengthen the sand pack and improve monitoring techniques. Among these materials are garnet sand (Wilkerson et al., 1992), silica powders (Bonnet et al., 2007; Galland et al., 2006), glass microbeads (Bonnet et al., 2008; Hoth et al., 2007), glass or aluminum microspheres (Rossi and Storti, 2003), mica flakes (Storti et al., 2000), Pyrex grains (Baby et al., 1995) or walnut shells (Cruz et al., 2008). In geomorphic experiments, granular materials are generally sandy particles or fine powders systematically dampened with water.

There are natural sands (Schumm et al., 1987; Wittmann et al., 1991), sand/silt/clay mixtures (Bryan et al., 1998; Flint, 1973; Gabbard et al., 1998; Koss et al., 1994; Pelletier, 2003; Phillips and Schumm, 1987; Schumm and Parker, 1973), loess (Lague et al., 2003; Rieke-Zapp and Nearing, 2005), artificial flyashes (Hancock and Willgoose, 2001) or silica powders (Babault et al., 2005; Bonnet, 2009; Bonnet and Crave, 2003; Crave et al., 2000; Rohais et al., 2011; Turowski et al., 2006). Graphite powders are also used to model coastal stratigraphy (Heller et al., 2001; Paola et al., 2001) whereas plastic powders are used to study the evolution of submarine canyon morphology (Lancien et al., 2005; Metivier et al., 2005).

In a previous work, a new experimental device and protocol based on both "tectonic" and "geomorphic" set-ups (Fig. 1c) (Graveleau and Dominguez, 2008) was presented. Objectives were to study the morphological evolution of an active piedmont controlled by the interactions between accretionary wedge deformation mechanisms and coeval erosion-transport-sedimentation processes. In the present paper, it is focused on the characteristics of the specific material developed to model simultaneously orogenic wedge deformation mechanisms (faulting, folding) and realistic surface processes (incision, hillslope processes). First, it was detailed and discussed the specifications and required physical properties. Second, the four granular media that compose the selected material was described. Then, the typical morphologic, tectonic and sedimentary features obtained with this material were analyzed. Finally deformation and erosion-transport processes and model scaling was discussed.

2. Specifications and required physical properties of model materials

2.1. Deformation and surface processes in models

Deformation of rocks in the upper continental crust is brittle and responds to the Mohr-Coulomb failure criterion (Byerlee, 1978). In mountain belt piedmont, the deformation is essentially localized along imbricated thrusts that dip toward the hinterland and branch on deep crustal

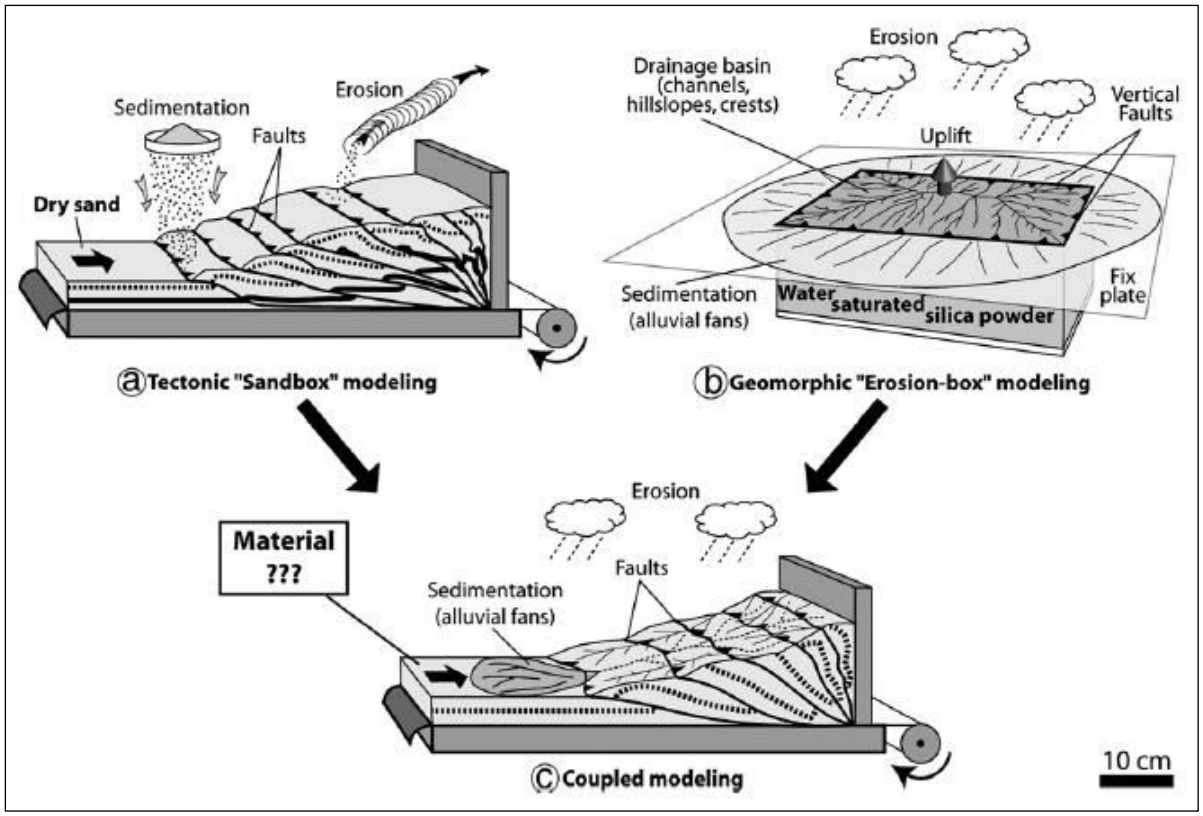

Figure. 1. Analog modeling of interactions between tectonics, erosion and sedimentation. (a) Typical tectonic "sandbox" set-up used for studying fold-and-thrust belts and orogenic wedge dynamics (Davis et al., 1983). It uses dry granular materials (typically, sand). Erosion is simulated by scrapping off material from relief whereas sedimentation is obtained by sifting fresh particles in basins (Konstantinovskaia and Malavieille, 2005). (b) Typical geomorphic "erosion box" set-up used for studying the dynamics of topography (Babault et al., 2005; Lague et al., 2003). A block of moistened powder (loess or silica powder) is uplifted vertically and eroded by sprinkling water micro-droplets over surface model. Sedimentation occurs over a surrounding plateau at the base of the topography. (c) Experimental set-up used in this paper to study interactions between tectonic and surface processes in an active foreland (Graveleau and Dominguez, 2008). It combines orogenic wedge deformation from set-up "a" and surface processes modeling by water runoff from set-up "b".

decollements (Molnar and Lyon-Caen, 1988; Suppe, 1981). It generates wedge-shape geometry and indicates the forward propagation of deformation toward the undeformed foreland (Chapple, 1978; Davis et al., 1983). In "sandbox" experiments, such deformation mechanisms, style and sequence are well reproduced with dry granular materials (Fig. 1a) (Davis et al., 1983; Malavieille, 1984; Mandl et al., 1977). In the model, it is expected that such an accretionary wedge deformation style and such sequences of thrust nucleation and propagation.

Mountain belt topography is shaped by a variety of surface processes that are mainly controlled by topographic slopes (Montgomery and Brandon, 2002). Generally, high slopes are observed at elevated topography and are shaped by specific hillslope processes (rockfall, landslides, debris flows, slumping) whereas low slopes lay at low elevation and are dominated by fluvial processes. Sedimentation occurs essentially in foreland flexural basins (Jordan, 1981) and piggy-back basins (Ori and Friend, 1984) where the decrease in river transport capacity brings sediment load to deposit. In "morphologic" experiments, erosion and transport processes are usually triggered by sprinkling water droplets over the model (Fig. 1b). Overland flow generates runoff detachment in channels (Lague et al., 2003) and may trigger landslides (Bigi et al., 2006). Similarly, it is expected that in the model such active geomorphic processes on hillslopes and along channels to generate realistic geomorphic patterns made of drainage networks, hillslopes, channels and alluvial fans.

As in nature, hillslope processes in this model should result from slope destabilization induced by river incision at hillslope toe or by fluid infiltration. Rain splash effect triggered by water

droplet impacts was avoided because it generates an unrealistic mechanical erosion process that destroys the morphological sharpness of drainage basins, channel networks and alluvial fans. As fluid transitory overpressures are negligible in fine sandy wedge models (Mourgues and Cobbold, 2006), destabilization processes on hillslopes are mainly controlled by the ratio between cohesive and body forces. To promote slope failures, body forces should be larger than cohesion and frictional properties. This requirement corresponds to materials with high particle density, low surface roughness, high sphericity, large grain-size, high permeability and high water saturation ratio. To reduce capillary forces that generate cohesion, liquid in material should have low surface tension and high density and should be near saturation.

Concerning channelized processes, water flow in channels can erode the substrate if the basal shear stress applied by the fluid on the riverbed exceeds the thresholds for detachment and transport (Howard, 1994). Threshold conditions are more readily met when infiltration is reduced (Lague et al., 2003). For granular materials, fluid infiltration capacity is controlled by permeability that is itself a function of grain-size distribution and porosity (Carman, 1938, 1956; Kozeny, 1927). Porosity is additionally a function of grain size, grain shape and packing. Therefore, to promote runoff, physical properties like grain size, porosity and permeability should be reduced. However, grain-size should not be excessively reduced, because cohesion generated by electrostatic forces or capillarity increases significantly for very small particles (Lague et al., 2003), thus increasing detachment threshold and reducing hillslope processes. In addition, particles are more easily detached and transported by runoff if the particle density is low and size of grains is small.

Finally, layering of deposited sediment is a desirable property to favor the study of syntectonic sedimentary record. It was sought for wide grain-size distributions, contrasted particle densities and grain shapes to promote transport dynamics that generate various transport distances of particles and create lateral facies changes in deposits.

2.2. Scaling

Experimental modeling is ruled by a set of geometric, kinematic and dynamic similarity criteria that imply, respectively, proportionality of length, time and forces between nature and model (Hubbert, 1951; Ramberg, 1981). Tectonic processes are scaled down using Cauchy's equations of motion for continuum medium in a non-dimensional form (Davy and Cobbold, 1991). It produces dimensionless numbers that must be preserved between nature and experiment (Horsfield, 1977; Weijermars and Schmeling, 1986). One of these (Froude number), links inertial to gravity forces. It is neglected because tectonic velocities in nature are slow (in cm/yr) compared to timescales of tectonic processes (in Myr). Another dimensionless number links body to surface forces. Its conservation between model and experiment leads to the expression:

$$\sigma^* = \rho^* . \mathrm{g}^* . L^* \qquad (1)$$

where σ^*, ρ^*, g* and L^* are the model to nature ratio for stress (or cohesion), density, gravity and length, respectively. It implies that cohesion, density, gravity and characteristic length scales in model should be proportionally linked to natural values. Generally, most experiments are performed in a normal gravity field, so g* equals 1. In addition, length ratio L^* is imposed by set-up dimensions and typically ranges around 10^{-5} (1cm= 1000m). Dry quartz sand satisfies these constraints since the angle of internal friction is typically in the range of natural rocks (around 25-45°), and the density ($\boldsymbol{\rho}$ = 1.5-1.7 g.cm^{-3}) and cohesion (10-100 Pa) present reasonable values to satisfy Eq. (1).Notethat few experiments have used moist sands (Chamberlin and Miller, 1918; Macedo and Marshak, 1999; Van Mechelen, 2004; Wang and Davis, 1996) because the addition of small amount of water increases the mechanical strength (Halsey and Levine, 1998; Hornbaker et al., 1997; Mitarai and Nori, 2006). It creates interstitial liquid bridges between particles that generate capillary forces and increase cohesion (Pierrat and Caram, 1997; Rumpf, 1962; Schubert, 1984). By controlling this increase in cohesion, it is possible to model continental crustal strengthening (Van Mechelen, 2004; Wang and Davis, 1996).
Downscaling geomorphic processes from nature to model is difficult (Lague et al., 2003; Niemann and Hasbargen, 2005; Paola et al., 2009; Peakall et al., 1996; Schumm et al., 1987). The problem is to simultaneously downscale the length, force and time boundary conditions without introducing scale distortions (Bonnet and Crave, 2006; Turowski et al., 2006). In nature, erosion and transport processes

occur over a wide range of time-scales (from rapid landslides or river floods to slow hillslope creep) and space-scales (sediment grain size ranges from micrometric particles to decimetric boulders). Experimentally, a rigorous reduction of these scales is impossible as it would require the use of nanometric particles and induce the occurrence of extremely rapid geomorphic processes (Bonnet and Crave, 2006; Schumm et al., 1987). However, the dynamic similarity of geo-morphic experiments has been recently addressed by comparing hydraulic dimensionless numbers (Reynolds and Froude numbers) between models and nature (Niemann and Hasbargen, 2005; Peakall et al., 1996). Reynolds number compares advective acceleration to frictional resistance (viscous forces) and distinguishes laminar (Re<500) and turbulent (Re>500) flow conditions. Froude number compares advective to gravitational accelerations and distinguishes subcritical (F_r< 1), critical (F_r= 1) or supercritical (F_r>1) flow conditions. Results indicate that Froude numbers in experiments compare well with natural values but Reynolds numbers are significantly lower. Although not perfectly scaled, this suggests however that the natural and experimental dynamics are both dominated by the same balance of forces. Gravitational forces are the leading forces in the system and they typically exceed inertial and viscous forces. This could be likely the reason explaining the striking similarity between natural and experimental landscapes that has been recently qualified as the "unreasonable effectiveness" of geomorphic experiments (Paola et al., 2009).

3. Suitable model materials

11 pure materials were tested in both dry and water-saturated conditions and then as mixtures so as to progressively approach a composition that fulfills the specifications previously described (Graveleau, 2008). For brevity, it was only presented in this paper the 4 granular media that compose the final material called "quaternary material" (MatIV). The 4 components are glass microbeads (GM), plastic powder (PVC), silica powder (SilPwd) and graphite powder (Graph). MatIV composition is made up with 40% of GM, 40% of SilPwd, 18% of PVC and 2% of Graphite (percentage in weight). In this section, it is essentially detailed their physical and mechanical properties in water-saturated conditions (Table 1). The measured properties are grain shape (sphericity, roughness), grain-size (median D_{50}), particle density ($\boldsymbol{\rho_{part}}$), bulk density of material ($\boldsymbol{\rho_{bulk}}$), porosity ($\boldsymbol{\theta}$)**,** permeability (k) and frictional properties (angle of internal friction $\boldsymbol{\theta}$ and cohesion C). All measurements were carried out at Jaypee HEW/HITECH Laboratory, Rewa, India.

Table 1: Physical properties of water-saturated granular materials. Parameters are median grain-size (D_{50}), density of particles ($\boldsymbol{\rho_{part}}$), bulk density of water-saturated material ($\boldsymbol{\rho_{bulk}}$), porosity ($\boldsymbol{\theta}$), water saturation ratio (w) and permeability (k). Frictional properties, i.e. the angle of internal friction (ϕ), the coefficient of internal friction (M) and the extrapolated cohesion (C) are determined for peak and stable friction. Permeability and frictional measurements have not been carried out for Graph as it is minor component of selected MatIV.

Materials	Sphericity	Roughness	D50 (μm)	ρ_{part} (g. cm	ρ_{bulk} (g. cm^{-3}) ±0.10	θ % ±1	w % ±1	k (m^2)	Peak friction			Stable friction		
									ϕ (°)	μ	C (Pa)	ϕ (°)	μ	C (Pa)
GM	Very high	Smooth	88	2.5	1.87	36	23	3.5×10^{-22}	36	0.73 ±0.07	0	31	0.60 ±0.06	0
SilPwd	Low	Rough	43	2.65	1.90	35	21	10^{-14}	58	1.62 ±0.40	5300 ±300	45	1.00 ±0.15	1300 ±300
PVC	High	Rough	147	1.38	1.11	46	63	7.2×10^{-12}	53	1.35 ±0.27	0	38	0.77 ±0.15	0
Graph	Low	Rough	172	2.25	1.42	35	31	-	-	-	-	-	-	-
Mat.IV	-	-	105	2.22	1.61	34	26	4.9×10^{-13}	48	1.13 ± 0.17	1200 ±200	40	0.83 ±0.12	750 ±200

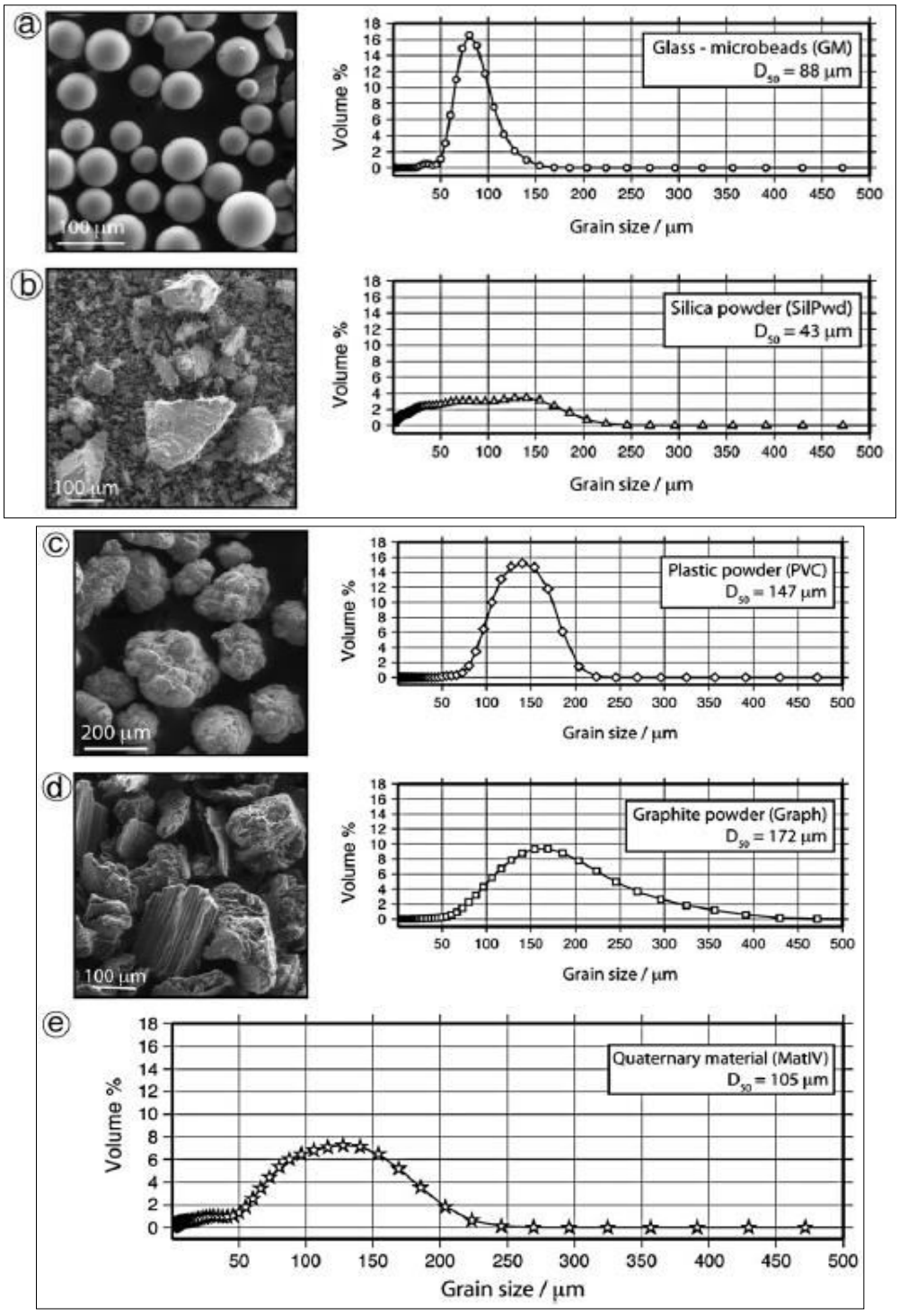

Figure. 2. Scanning electron micrograph pictures and grain size histograms of tested granular materials and selected composite material. Grain size data were obtained with a laser granulometer. (a) Glass microbeads (GM). Grains are highly spherical with a smooth surface. Grain size histogram ranges between 50 and 150 µm and nearly symmetric around D_{50} = 88µm. (b) Silica powder (SilPwd). Grains are angular in shape and have a wide size distribution from 1 to 250 µm with a D_{50} = 43 µm(c) Plastic powder (PVC). Particles are globular and range between 75 and 225µm. Median is D_{50} = 147µm. (d) Graphite powder (Graph). Grains are tabular and very irregular in shape. Grain size histogram ranges from 50 to 450 µm with a D_{50} = 172µm. (e) Quaternary material (MatIV). It is composed of the four previous materials. Its grain size distribution ranges from 1 to 250µm, with a D50 at 105µm.

3.1. Grain size and particle density

Each granular material was measured for shape and size with a scanning electron microscope and a laser granulometer, respectively (Fig. 2; Table 1). GM (Eyraud S.A, France) has a grain size between 50 and 150 Mm with a median D_{50} at 88 Mm (Fig. 2a). The grains are spherical and very smooth. The manufacturer gives a particle density around 2.5 ±0.1. SilPwd (SIBELCO FRANCE, France) has a grain size between 1 and 250 Mm with a D_{50} at 43 Mm(Fig. 2b). The grains are very angular and the particle density is 2.65 (pure quartz). PVC (Solvay S.A., France) has a grain size between 75 and 225 Mm with a median at 147 Mm(Fig. 2c). The grains are globular and their density is around 1.38 ±0.1 according to the manufacturer. Graphite (GraphTek S.A., France) has a grain size between 50 and 450 Mm with a D_{50} at 172 Mm (Fig. 2d). For this study, grain size between 90 and 250 Mm only were kept. The grains are angular and their density is 2.25 ± 0.1 according to the manufacturer. Finally, the selected MatIV has a grain size ranging from 1 to 250 MmwithaD$_{50}$at 105 Mm(Fig. 2e). It is possible to evaluate a mean particle density for MatIV ($<\rho_{\mathrm{Part-MatIV}}>$) by assuming an equation of volume conservation (Eq. (2)):

$$< \rho_{\mathrm{Part-MatIV}} >= \left(\frac{\chi_{GM}}{\rho_{GM}} + \frac{\chi_{SilPwd}}{\rho_{SilPwd}} + \frac{\chi_{PVC}}{\rho_{PVC}} + \frac{\chi_{Graph}}{\rho_{Graph}} \right)^{-1} \quad (2)$$

with

$$\chi_i = \frac{M_i}{M_{MatIV}}$$

χ_i is the mass proportion of pure component "i" in MatIV. According to this expression, MatIV has a mean particle density close to 2.22 ± 0.1. This value is used for erosion tests reported in the next section.

3.2. Average water-saturated bulk density

Average water-saturated bulk density for each material (ρ_{bulk}) was calculated by weighing successive known volumes of material (Cobbold and Castro, 1999) (Fig. 3a). As density is a function of compaction and handling technique (Krantz, 1991; Lohrmann et al., 2003), each test was carried out with a similar technique that consisted of mixing the material with a saturation proportion of water before filling containers of various volumes. Each sample was slightly vibrated to ensure air bubble escapement. Plot of mass versus volume indicates a good linear correlation whose slope equals density (Fig. 3b). Calculated densities are 1.87 ± 0.10 g/cm^3 for GM, 1.90 ± 0.10 g/cm^3 for SilPwd, 1.11 ±0.10 g/cm^3 for PVC, 1.42 ±0.10 g/cm^3 for Graphite and 1.61 ±0.10 g/cm^3 for MatIV (Table 1). It is stressed that these measured densities represent average values at the scale of large volumes and that bulk density can likely increase downward due to compaction (see discussion in Section 4.4).

3.3. Average porosity and water saturation rate

Porosity (**θ**) is defined as the volume of empty space within a sample relative to the total volume of the sample. Average porosity was measured for each water-saturated material by weighing a volume of material that was initially mixed with water, drying the sample in an air oven and weighing the sample again. The mass difference between the two measurements was assumed to represent the mass of water that initially filled pores and then evaporated. Saturation of materials was performed at atmospheric pressure with the same protocol as for bulk density. Only a few tests were performed for each sample, with consistent results. Porosity is 36 ±1% for GM, 35 ±1% for SilPwd, 46 ±1% for PVC, 35 ±1% for Graphite and 34 ±1% for MatIV (Table 1). These results are in the same range of values (±5-10%) as analytical calculations performed with measurements of particle density and bulk density (Graveleau, 2008).

Water saturation ratio (w) in granular media is the mass ratio of interstitial liquid (water) to solid (grains). Average saturation ratio from mass measurements, collected during porosity tests was calculated. It is 23 ±1% for GM, 21 ±1% for SilPwd, 63 ±1% for PVC, 31 ±1% for Graphite and 26±1%for MatIV(Table1).

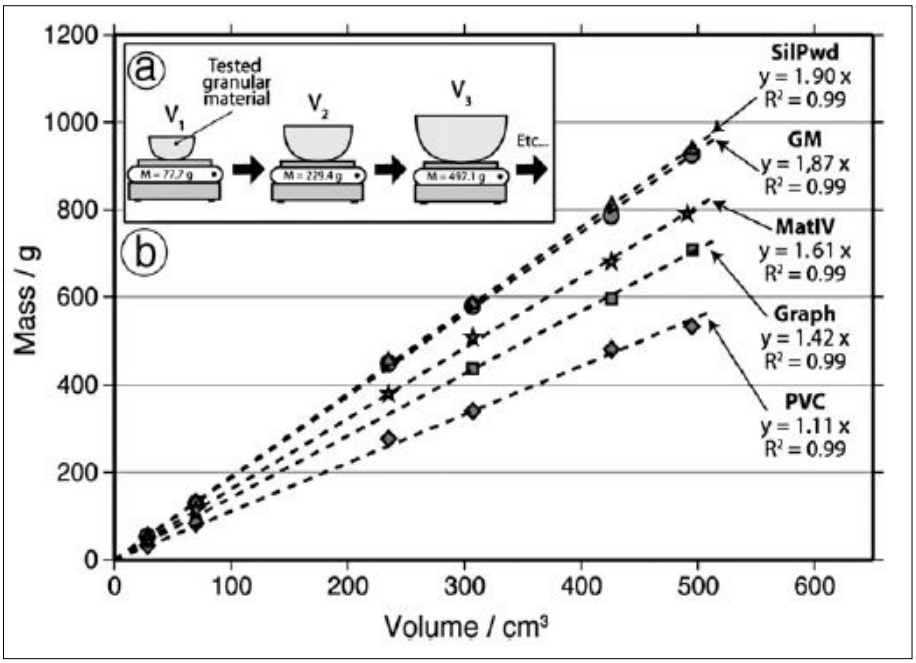

Figure. 3. Bulk density measurements for water-saturated granular materials: (a) Experimental protocol. It consists in measuring the mass of increasing volumes of materials. (b) Plots of mass versus volume for GM, SilPwd, PVC, Graph and MatIV. Slopes of best-fitted lines provide an estimation of bulk densities. It is 1.90 ±0.10 g.cm^{-3} for SilPwd, 1.87 ± 0.10 g.cm^{-3} for GM, 1.11 ±0.10 g.cm^{-3} for PVC, 1.42 ± 0.10 g.cm^{-3} for Graph and 1.61 ± 0.10 g.cm^{-3} for MatIV. Error bars are not indicated since they are smaller than symbol size.

3.4. Permeability

Permeability (k) is defined as the ability of a porous material to allow fluids to pass through it. It was measured with a Darcy pipe device made with a PVC cell filled with the tested material (Fig. 4a). Cell length (L) and section (S) were respectively 0.25 m and 5.43×10^{-4}m^2.An electric pump (accuracy 0.01 ml/h) supplied increasing water discharge stages (Q) at the entrance. Two pressure gauges (accuracy 100 Pa) measured the water pressure gradient at both pipe edges ($dP = P_{In} — P_{Out}$). Strainers, pressure equalizers and filter papers were arranged at the extremities of the cell to maintain

Well-known Darcy's law (Darcy, 1856) indicates proportionality between the discharge velocity (Q/S) of an incompressible fluid through a porous medium, and the longitudinal gradient of the fluid pressure (dP/L). For this experiments, assuming a one-dimensional flow, it gives (Eq. (4)):

$$\frac{Q}{S} = \frac{k}{\eta}.\frac{dP}{L} \qquad (4)$$

with η the dynamic viscosity of the fluid. A linear relationship between discharge velocity and the longitudinal pressure gradient indicates that the materials follow Darcy's law (Fig. 4b). Mean-square correlations give slopes k/η around 3.5×10^{-9} m^2/ Pa.s for GM, 7.2×10^{-9}m^2/Pa.s for PVC and 4.9×10^{-10} m^2/Pa.s for MatIV (Table1).Assuming a viscosity of $\eta = 10^{-3}$Pa.sforwater, permeability is around 3.5×10^{-12}m^2 (3.5 Darcy) for GM, 7.2×10^{-12}m^2 (7.2 Darcy) for PVC and 4.9×10^{-13} m^2 (0.5 Darcy) for MatIV (Table 1). The protocol was inappropriate for SilPwd because it has a very low permeability below experimental determination. However, it was estimated that an order of magnitude around 10^{-14} m^2 (0.01 Darcy) from one single measurement of water discharge and pressure gradient. Graphite was not measured, since it represents a minor proportion of the selected composition. All measurements are consistent with permeability calculated for moistened silica powder in geomorphologic experiments ($k=10^{-14}$m^2) (Rohais, 2007) and for dry sand in tectonic experiments ($k=10^{-11}$-10^{-10} m^2) (Cobbold etal., 2001).

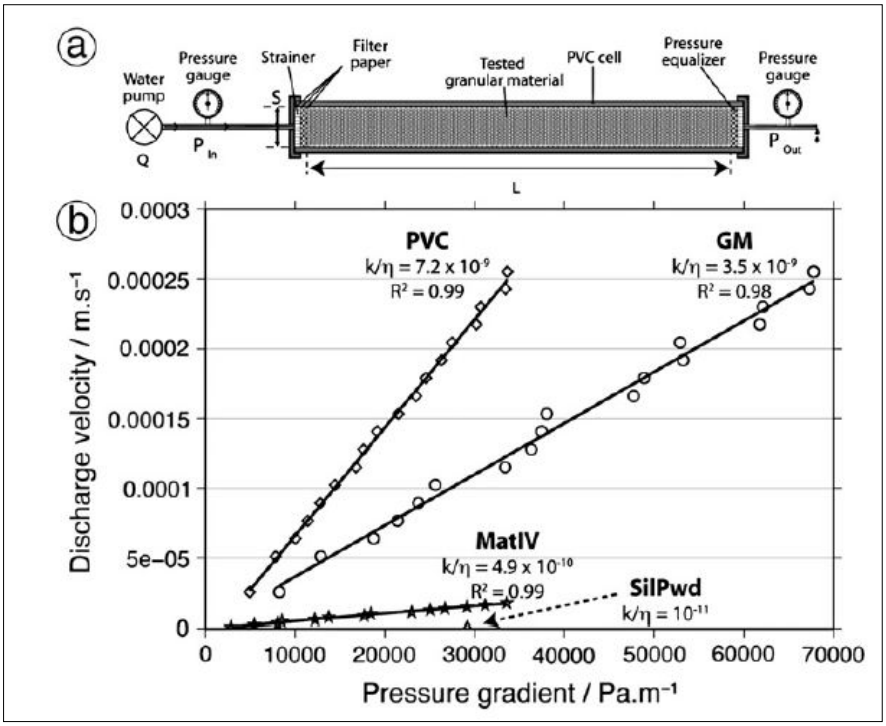

Figure. 4. Permeability measurements. (a) Experimental permeameter. It consists in measuring the water pressure gradient at the edge of a cylindrical cell (P_{In} and P_{Out}) receiving various water discharges as input (Q). (b) Plots of water discharge velocity (inm.s^{-1}) ver-sus longitudinal pressure gradient (inPa.m^{-1}). Given water viscosity (10^{-3} Pa.s), best-fit lines yield permeability for each granular material according to Darcy's law. Permeability for GM, PVC, SilPwd and MatIV are respectively 3.5×10^{-12} m^2, 7.2×10^{-12} m^2,10^{-14} m^2 and 4.9×10^{-13} m^2. Graphite permeability has not been measured. Error bars are smaller than symbol size.

3.5. Deformation behavior

3.5.1. Frictional properties

Granular materials deform according to the linear Mohr-Coulomb criterion that links shear stress $\boldsymbol{\tau}$ to normal stress σ_n on the failure plane (Eq. (5)).

$$\tau = \mu . \sigma_n + C \quad (5)$$

where C is cohesion and μ is the coefficient of internal friction defined by $\mu = \tan \phi$, where ϕ is the angle of internal friction. Frictional properties are determined with various apparati that measure shear stress at failure for increasing normal stresses. These devices are the Hubbert-type set-up (Cobbold and Castro, 1999; Cobbold et al., 2001; Galland et al., 2006; Hubbert, 1951; Krantz, 1991; Lohrmannet al., 2003; Mourgues and Cobbold, 2003; Richefeu et al., 2006, 2007; Schellart, 2000; Van Mechelen, 2004), the Casagrande shear box (Casagrande, 1932; Rossi and Storti, 2003), and the ring shear tester (Adam et al., 2005; Ellis et al., 2004; Hampel et al., 2004; Hoth et al., 2007; Mandl et al., 1977; Panien et al., 2006; Schulze, 1994). Coefficient of internal friction μ corresponds to the slope of the regression curve (yield locus) of couples $(\boldsymbol{\sigma_n, \tau})$ defined at failure. Cohesion C corresponds to the extrapolated shear stress at zero normal stress. This extrapolation slightly overestimates cohesion since the yield locus is curved downward at very low normal stresses (Schellart, 2000). Finally, the frictional properties of an undeformed material are generally different from those of an already deformed material (Byerlee, 1978; Lohrmann et al., 2003; Mandl et al., 1977). The higher strength of an undeformed material defines "peak friction" conditions whereas the lower strength of the already deformed material defines the "dynamic-stable friction" conditions.

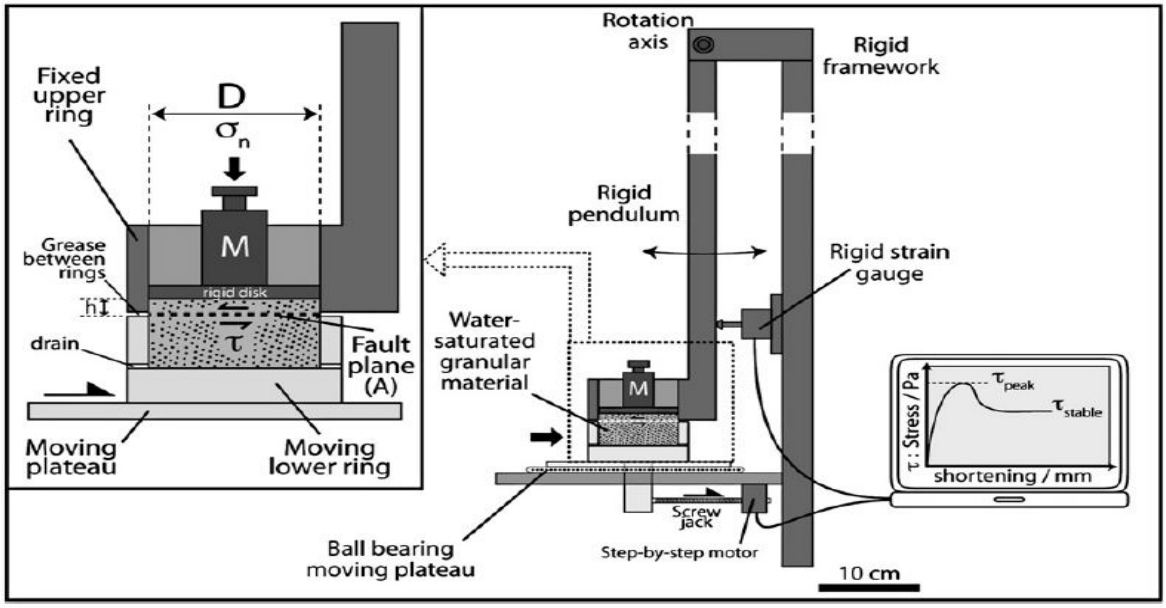

Figure. 5. Schematic sketch of shear box set-up. It is a Hubbert-type apparatus (Hubbert, 1951) composed of two rigid rings that contain the water-saturated sample. The lower ring is mobile and driven by a computerized stepping motor. The upper ring is fixed on a rigid framework. It is equipped with a force gauge to measure the shear force required to fracture the granular material. Each material is tested with increasing normal stresses (from 500 to 4000 Pa) provided by standard mass M settled over the sample.

3.5.1.1. Experimental facility and protocol.

A modified Hubbert-type direct shear apparatus was built to measure the frictional properties of the water-saturated granular materials (Fig. 5). It consists of two aluminum rings, 8 cm in internal diameter (D) and 50 cm^2 in horizontal cross-sectional area (A), which contain the granular material sample.

The lower ring is 3 cm deep and perforated to drain the sample. It is fixed on a mobile plateau whose displacement is controlled by a stepping motor. The upper ring is 5 cm high and fixed on a rigid pendulum that rests on a force gauge. Its internal surface is covered with a low friction film to reduce sidewall friction. A 0.1 mm gap between both rings avoids their contact and controls the location of the shear plane. This gap is filled with low viscosity grease to prevent material and water from escaping. Several tests carried out with the empty shear box and involving (or not) grease indicate that the viscous forces added by the grease film are negligible relative to the shear force required to deform samples. When the lower ring moves rightward, the granular sample is sheared and The upper ring presses the force gauge. Both displacement and force gauge data are continuously recorded and allow calculating stress-strain curves (Fig. 5).

In these tests, the total displacement of the lower ring is 5 mm, which is enough to shear the sample and generate a fault plane. During this displacement, the cross-sectional area (A) between the upper and lower ring and within the sample is not constant and decreases progressively to reach a maximum of about 8% at the end of the test. The force measurements therefore include some frictions of the ring borders within the sample, which likely drives to a slight underestimation of friction. In each test, the sample height (h) of material above the failure plane is 10 ±0.5 mm. For most materials (i.e., GM, PVC and MatIV), this thickness is large enough to avoid internal deformation and low enough to avoid sidewall friction. The height to diameter ratio h/D = 0.125 is well below the 0.6 limit over which Jansen correction for sidewall friction should be considered (Mourgues and Cobbold, 2003). Note that this limit has been estimated for dry sand, but it is assumed that it should be similar for water-saturated materials. Measurements with SilPwd were more difficult because this material is very cohesive. A10 mm high sample was too thick to avoid sidewall friction, but it was impossible to reduce the height of the sample otherwise internal deformation was observed. Consequently, although

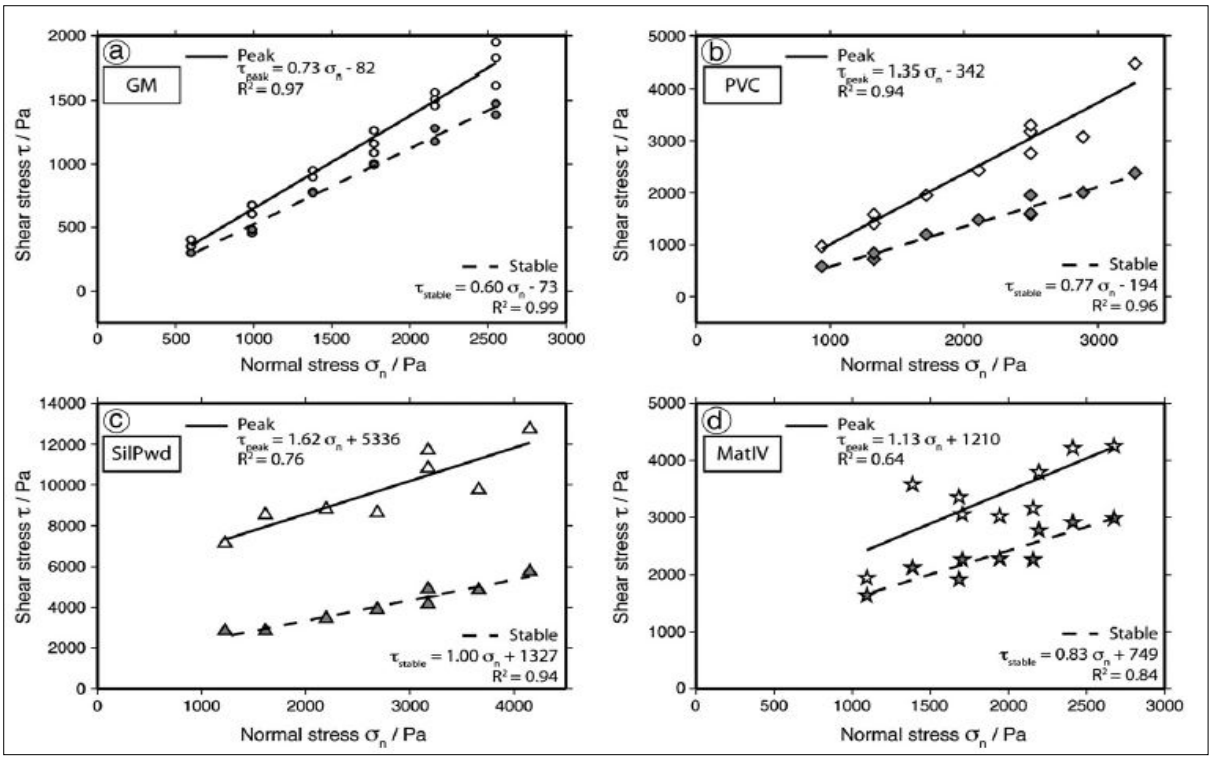

Figure. 6. Mohr-Coulomb envelopes for failure of (a) GM, (b) PVC, (c) SilPwd and (d) MatIV. Open symbols correspond to peak friction measurements and full gray symbols correspond to stable friction measurements. Each data set falls into line according to Mohr-Coulomb failure criterion. Best-fit slopes and intercept at zero normal stress define the coefficient of internal friction (μ) and cohesion (C) respectively.

this tests produce consistent data to deduce a yield locus curve (see below), they must be considered as approximate. It is particularly pointed out that these tests give minor values for cohesion and friction and provide an order of magnitude estimate.

Several tests with increasing normal loads were performed to measure normal and tangential stress couples at failure and deduce a yield locus. The normal load applied on the shear plane corresponded to the sum of the sample material in the upper ring (m = ρ.A.h), a rigid disc (m_{disc} = 209 g) and a standard mass M (Fig. 5). Each failure test was performed with the same mass of material and rigid disc, under constant measured saturation states but with increasing standard masses (from 500 g to 3000 g). Normal and measured shear forces were converted to normal and shear stresses by dividing by the shear plane area (A). They were in the range of 500-4000 Pa, which is slightly above typical normal stresses in dry shear tests of the literature (most are around 0-1500 Pa).

Finally, materials were settled in the rings with the same protocol as for density and porosity measurements. Samples were totally removed and replaced by new material for each test. As frictional properties of granular materials depend strongly on the conditions of preparation, bulk material density and water saturation ratio was systematically measured. Both were in the range of values reported in Table 1.

3.5.1.2. Experimental results.

The results indicate that a Mohr-Coulomb failure envelope can be drawn for the four tested materials at both "peak friction" and "stable friction" (Fig. 6). The best linear fit to the data gives a slope equal to the coefficient of internal friction \x, and an extrapolated cohesion C. Results for each material are summarized in Table 1, except for Graphite, which was not measured. For GM, coefficient of peak friction is $\boldsymbol{\mu_{GM-peak}}$= 0.73 ± 0.07 (i.e., $\boldsymbol{\phi_{GM-peak}}$= 36°) and coefficient of stable friction is $\boldsymbol{\mu_{GM-stable}}$ = 0.60 ± 0.06 ($\boldsymbol{\phi_{GM-stable}}$ = 31°) (Fig. 6a). Both peak and stable extrapolated cohesions are negative and therefore assumed to be close to 0 Pa (respectively $\boldsymbol{C_{GM-stable}}$= —82 Pa

and $\mathbf{C_{GM-stable}}$= — 73 Pa). For PVC, coefficients of peak and stable friction are high ($\boldsymbol{\mu_{pvc-peak}}$ =1.35± 0.27; that is $\boldsymbol{\phi_{pvc-peak}}$= = 53°; $\boldsymbol{\mu_{pvc-stable}}$= 0.77 ± 0.15; that is $\boldsymbol{\phi_{pvc-stable}}$ = 38°) (Fig. 6b). Extrapolated cohesions are also negative and assumed to be virtually null ($\mathbf{C_{pvc-peak}}$= — 342 Pa and $\mathbf{C_{pvc-stable}}$= —194 Pa). For both GM and PVC, it was assumed that measured negative cohesions are due to slight overestimations of normal stresses triggered by non-zero sidewall friction. For SilPwd, yield locus is well constrained for stable conditions but not for peak conditions as indicated by correlation coefficients (0.94 and 0.76 respectively) (Fig. 6c). They are respectively around $\mu_{SilPwd-peak}$ = 1.62 ± 0.40 (that is $\phi_{SilPwd-peak}$ = 58°) and $\mathbf{C}_{SilPwd-peak}$ = 5300 ± 500 Pa for peak conditions and $\boldsymbol{\mu}_{SilPwd-stable}$ = 1.00±0.15 (that is $\boldsymbol{\mu}_{SilPwd-stable}$ = 45°) and $\phi_{SilPwd-stable}$ = 1300± 500 Pa for stable conditions. Extrapolated cohesions are very high compared to GM or PVC, which is consistent with observations made when handling and deforming the material. Finally, selected MatIV presents high coefficients of internal friction for peak friction ($\mu_{MatIV-stable}$=1.13±0.17; that is $\phi_{MatIV-stable}$ = 48°) and stable friction ($\mu_{MatIV-stable}$= 0.83 ±0.12; that is $\phi_{MatIV-stable}$ = 40°) and high value of extrapolated cohesion ($C_{MatIV-peak}$= 1200 ± 500 Pa and $\mathbf{C}_{MatIV-stable}$=750±500Pa) (Fig. 6d). These values for MatIV will be discussed later in regards to scaling issues.

It is difficult to compare these results with published values as very few experimental works deal with this kind of water-saturated materials. In the geosciences literature, a water-saturated mixture made of sand, silt and kaolinite was measured with a cohesion around 112.5 Pa (Shepherd and Schumm, 1974) but no information was given on the measurement protocol. More recently, apparent cohesion for under-saturated sands in the pendular state (i.e. the phase where the liquid between grains is discontinuous) was measured between 100 and 5000 Pa (Van Mechelen, 2004). In the civil engineering literature, experimental works refer generally to low water content (up to 4-5%). The angle of internal friction of granular materials is supposed to be constant as a consequence of moistening (Pierrat et al., 1998) whereas cohesion increases with water content until it reaches a plateau (Richefeu et al., 2006). This cohesion plateau is around 800 Pa for sands and glass beads between 100 and 500 μ_m in diameter (Richefeu et al., 2006, 2007; Soulie et al., 2006).

3.5.2. Deformation style

Each water-saturated material was tested in a classic sandbox setup to analyze the deformation style and mechanical behavior (Fig. 7). Cross-sectional pictures taken at a similar state of deformation was presented, which corresponds to 30 cm of shortening. Experimental runs lasted several tens of minutes during which overpressures were supposed to be negligible due to material permeability (Mourgues and Cobbold, 2006). The basal friction was high ($\mathbf{\mu_b}$= 0.5) in all tests and no material was allowed to output the system. Rainfall was absent so the "aerial" part of the rising wedge was likely under-saturated as water was allowed to percolate through the pores down to the base level. However, saturation state was maintained in the incoming thickness of material using a water tank located behind the buttress (Fig. 7a). These experimental conditions were chosen to focus the study on deformation style and therefore differ slightly from standard geomorphic experiments detailed in the discussion section (Fig. 12). Depending on material permeability, it is presumed that the under-saturation of the aerial part of the wedge only slightly modify deformation styles.

These results confirm that deformation of water-saturated materials generate accretionary wedges with thrust planes dipping toward the rigid buttress and propagating sequentially outward (Davis et al., 1983). However, deformation styles are different between materials. GM and PVC present few well-individualized thrusts and back thrusts (4 to 5) and relatively low surface slope **a** (10 ±0.5° for GM (Fig. 7a') and 7.5 ±0.5° for PVC (Fig. 7b')). GM has a significant component of deformation by folding above the most external thrust (#4), whereas PVC mostly deforms brittlely (see for instance the occurrence of back-thrusts over ramp #4). On contrary, SilPwd presents a much more brittle deformation style with 7 main thrusts and numerous back-thrusts (Fig. 7c'). The taper slope is high (around 14±0.5°). Finally, MatIV displays a deformation style characterized by 5 well-individualized thrusts and few back-thrusts (Fig. 7d'). Surface slope is high (15 ±0.5°). According to these tests, the deformation style for GM, PVC and MatIV reproduces well an accretionary wedge pattern made of individualized in-sequence thrust faults dipping toward the buttress whereas SilPwd displays small, very numerous and closely spaced thrusts. This is certainly due to its higher cohesion than GM, PVC and MatIV (see Section 3.5.1.2).

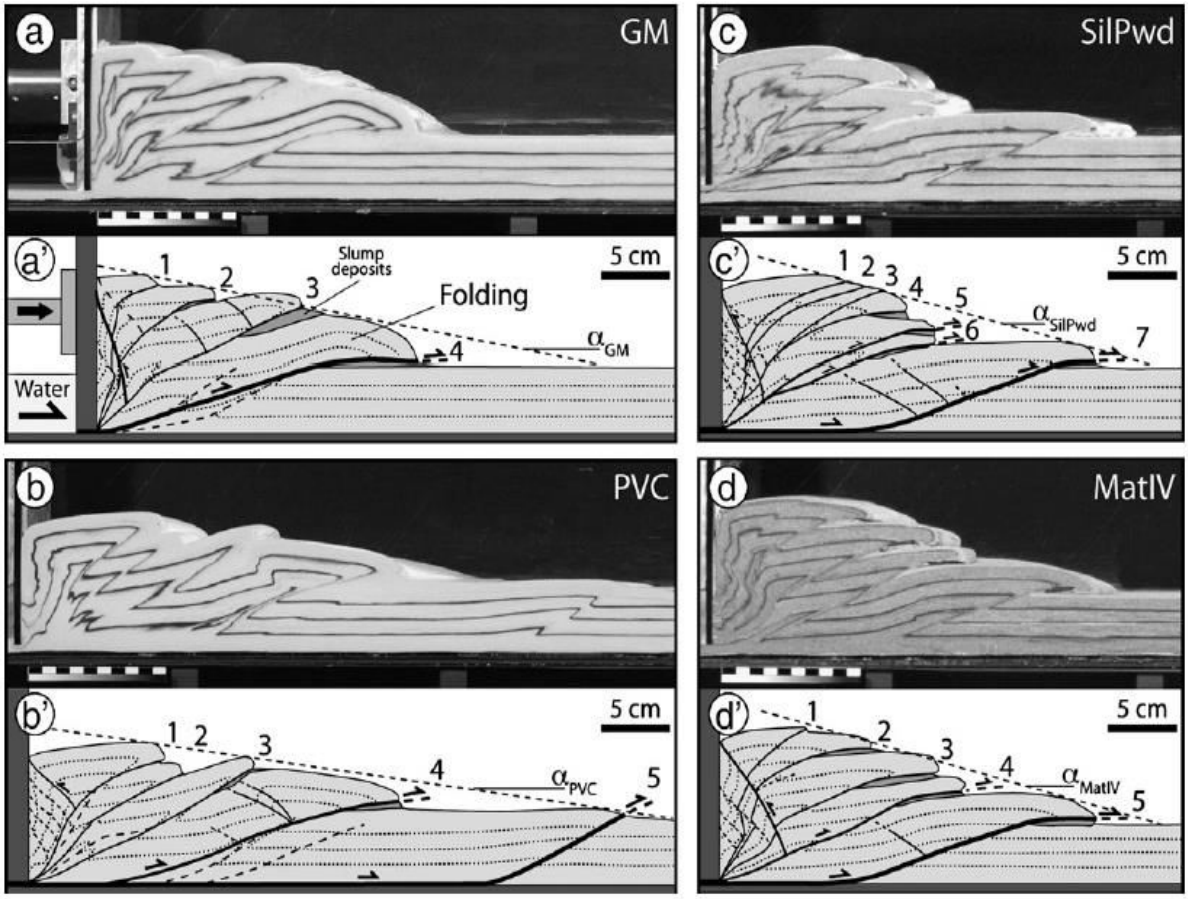

Figure. 7. Deformation style for water-saturated granular materials. Pictures are in cross-section and represent the final stage after 30 cm of shortening. Note the difference in deformation style between (c) SilPwd (many thrusts and back-thrusts) and other materials (fewer thrusts, folding).

3.6. Erosive properties

3.6.1. Experimental set-up and protocol

An experimental set-up was built to analyze the surface morphology and erosion-transport properties of each water-saturated material (Fig. 8). It is quantified that sedimentary fluxes in order to calculate mean erosion rates and derive erosion law parameters. The measurement protocol is based on several previous techniques (Hasbargen and Paola, 2000; Metivier and Meunier, 2003) and consists of a PVC box (0.358 m long, 0.347 m large and 0.050 m deep) filled with water-saturated material. It can be tilted by an angle a from few degrees to 30°. A rainfall system delivers water micro-droplets (precipitation rate around 25-30 mm/h; mean droplet diameter near 100 Mm) that trigger erosion-transport of the material. Calculation of impact kinetic energy released by micro-droplets shows that their energy is below the natural range of grain-grain binding energy (5-600 μ_J) (Lague et al., 2003; Salles et al., 2000). Rain splash is therefore limited and erosion occurs mainly by surface runoff and/or mass slides. Eroded particles flow down the slope and fall in a settling tank (tank 1). This tank is filled with water and its volume is maintained constant using an overflow device. As eroded particles fall in tank 1, they replace a volume of water that overflows in a second tank (tank 2). Two mass balances (accuracy 0.1 g) measure the weight of both tanks. The first balance at tank 1 measures the cumulative mass of eroded sediment whereas the second one at tank 2 controls the amount of supplied water. All experiments are prepared using a similar protocol. First, the material is saturated with water and then poured in the box. Excessive material is delicately scraped off and leveled with a ruler. Secondly, the material is allowed to settle overnight so that some water can evaporate and allow the model to sustain future tilting. Finally, the model surface is tilted by a fixed angle at the beginning of the experiment and the rainfall precipitation is initiated.

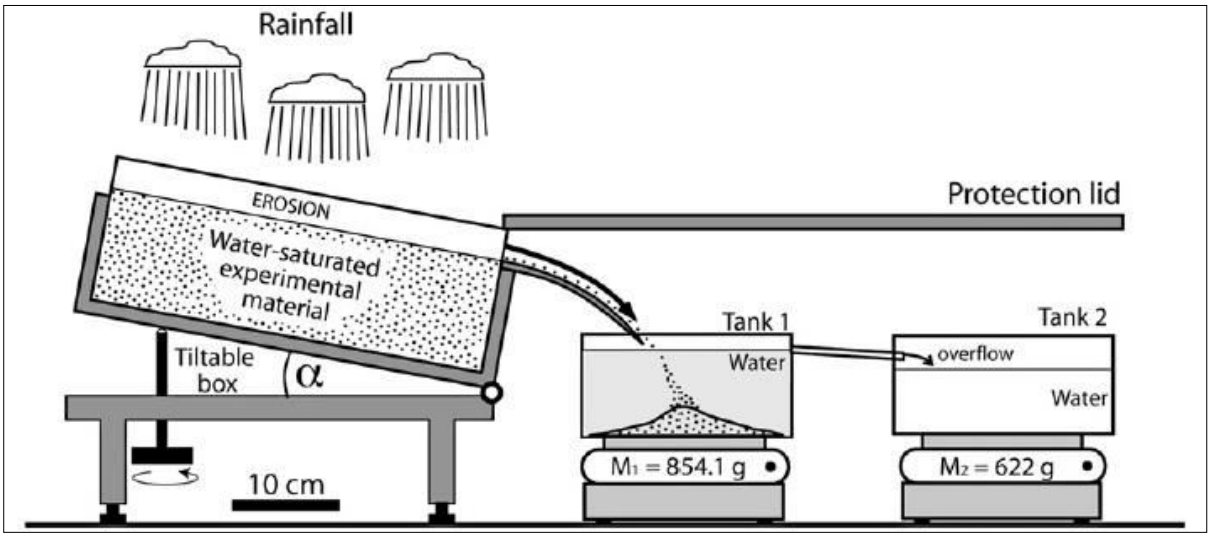

Figure. 8. Experimental set-up for measuring erosion flux of water-saturated materials. A box is filled with material and tilted by an angle a. Rainfall precipitation above the experimental box erodes the surface. Eroded particles fall in a tank filled with water (tank 1) and excessive liquid overflows in a second tank (tank 2). The evolution of tank masses is recorded with two accurate balances. A protection lid prevents precipitation from falling directly in tanks 1 and 2.

3.6.2. Basic landforms and fluxes

Four experiments were presented which was performed with a constant surface slope of 15° to illustrate how materials erode (Fig. 9). This slope is imposed as an initial stage by tilting the erosion box (Fig. 9a). Such experiments correspond to topographic relaxation tests as no additive tilting is applied afterwards (Crave et al., 2000; Lague et al., 2003). The results were discussed for each material by describing first the final stage morphologies and second their recorded mass evolution curve (sediment yield). Note that pictures were taken at different times (15min for PVC, about 1 or 2 h for GM and SilPwd, and 6h for MatIV) because materials erode at various erosion rates. Qualitatively, the morphology observed in pure material experiments is significantly different when comparing GM or PVC (Fig. 9b and c) with SilPwd or MatIV (Fig. 9d and e). GM and PVC have a wide 15° tilted plateau preserved in the uppermost part of the drainage basin where no erosion occurred. The lower part is poorly channelized and corresponds to slightly tilted surfaces. Their slopes were measured at 9.7-10.1 for GM and 2.4-2.9 for PVC with a digital inclinometer (accuracy 0.1°). In both cases, the erosion front displays concave scarps that indicate erosion processes dominated by landsliding. The absence of overland flow suggests that precipitation is lower than infiltration capacity. All precipitated water seeps through material pores and generates subsurface flow. The impermeable bottom of the box directs the flow lines toward the outflow device, and subsurface flows weaken the base of the erosion front, triggering landslides and mass wasting. This hypothesis is supported by high values of measured permeability for GM and PVC reported above (Table 1). SilPwd displays a channelized drainage pattern with at least five main catchments delimited by tortuous crestlines (Fig. 9d). Some relics of the initial tilted plateau are still preserved along the upper borders but their surface is small. The downstream zone has a homogeneous slope of 10-10.3 and is composed of deposited particles or outcropping "bedrock". The transition zone between channels and hillslopes displays frequent overhanging banks that can be removed by landslides. Finally, MatIV presents six well-defined drainage basins with remnants of the initial surface along the upper border and crestlines between each of them (Fig. 9e). Overhangs on hillslopes are rare because landslides frequently remove them. In the middle section, bedrock and alluvial terraces formed due to the lateral and upstream incision of streams. The downstream domain displays a tilted zone with "alluvial" and "bedrock" portions dipping at a mean slope around 8 ± 0.2°. In all these examples, the tilted downstream surface could have evolved as a "buffer zone", that is, it regulated the incoming and outgoing fluxes of particles according to transport capacity. Or it could also have evolved as a "by-pass zone", that is, most of the particles eroded from above are simply transmitted along this surface

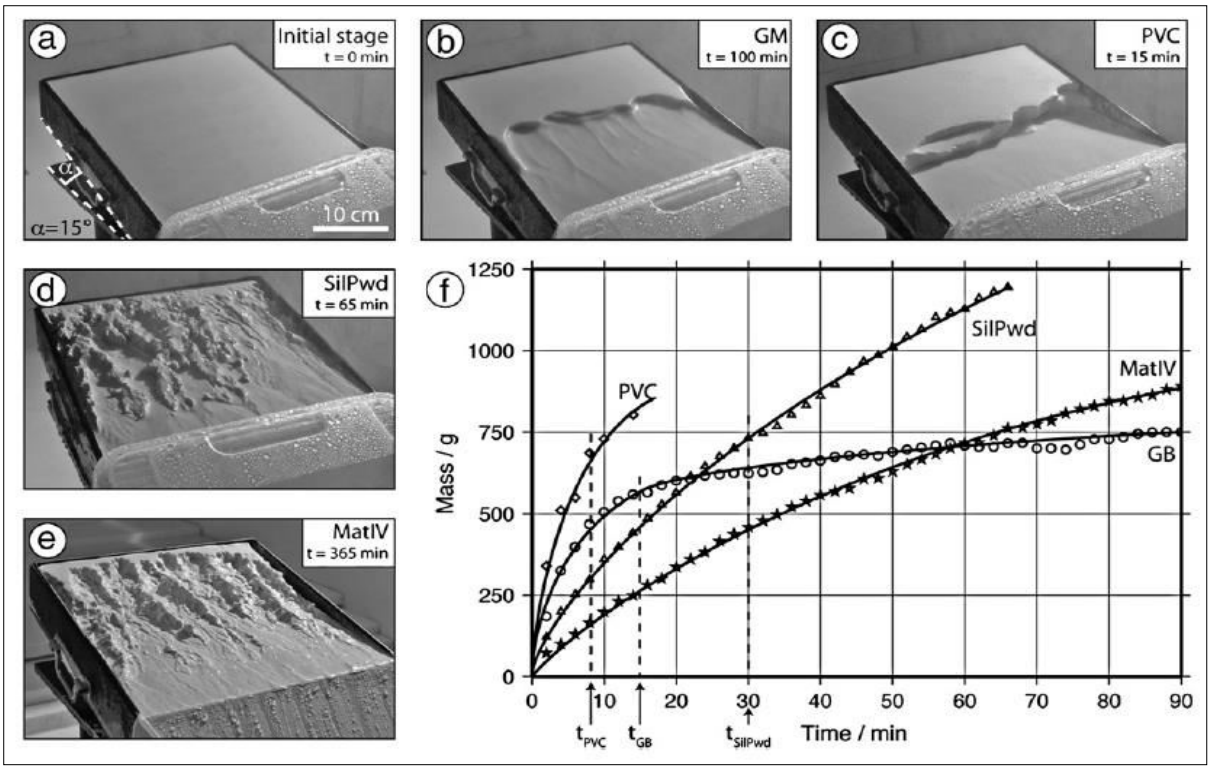

Figure. 9. Erosion morphology of water-saturated materials. Initial slope in each testis constant and equal to 15°. (a) flat tilted initial surface. (b) GM, (c) PVC, (d) SilPwd and (e) MatIV. Erosional patterns are significantly different between GM and PVC, on the one hand, and SilPwd and MatIV on the second hand, due to different erosion-transport mechanisms. Mass landsliding dominates for GM and PVC, whereas surface runoff and detachment dominates for SilPwd and MatIV. (f) Mass versus time evolution curves for each tested material. Characteristic times of change in curve evolution are mentioned and detailed in the text.

toward the overflow device. In the first case, the measured output flux may be a minimum estimation of the volume eroded in the drainage basins. In the latter case, it may fit more closely to the real eroded volume. In both circumstances, the dynamics of this downstream flat domain is likely related to thresholds in erosion and transport of particles (Lague et al., 2003).

The evolution of sediment yield for each material displays different trends and therefore indicates different erosion rates (Fig. 9f). For GM, the curve has a steep slope (about 49 ± 1 g/min) during the first 10 min, which rapidly decreases during the last hour (sediment yield around 2±0.1 g/min). The time of transition to stable phase t_{GM} is around 15 min. For SilPwd, the evolution curve is much more regular and grows with a relatively constant slope (16±1 g/min). However, a slight inflection is apparent around t_{SilPwd} = 30 min and splits the evolution into two phases. Mean sediment yield is around 22 ±1 g/min before this time, whereas it is about 13 ±0.1 g/min after. For PVC, the yield curve is much shorter as the experiment lasts only 15 min. The global trend of the curve defines a high mean sediment yield (35 ± 1 g/min) that can be divided into two sections: a rapid phase of sediment production during the first 5 min (88 ± 1 g/min) and a slight decrease around t_{PVC} =7-8 min (50 ±1 g/min). Finally, MatIV has a regular concave-down yield curve with a mean slope around 15 ±1 g/min during the first 20 min and around 5 ± 0.1 g/min for the last 30 min.

In conclusion, these tests indicate that water-saturated granular materials like PVC or GM display high erosion rates and favor mass wasting processes. This behavior is certainly related to the relatively high porosity and permeability and low cohesion. Under such conditions, no drainage basin and channel forms. SilPwd and MatIV favor incision processes and develop drainage basins and drainage networks with hillslopes and crests. The large granulometric dispersion of particles allows detailed morphological features in catchments. From a morphological point of view, PVC and GM do not fit the physical requirements but SilPwd and MatIV do.

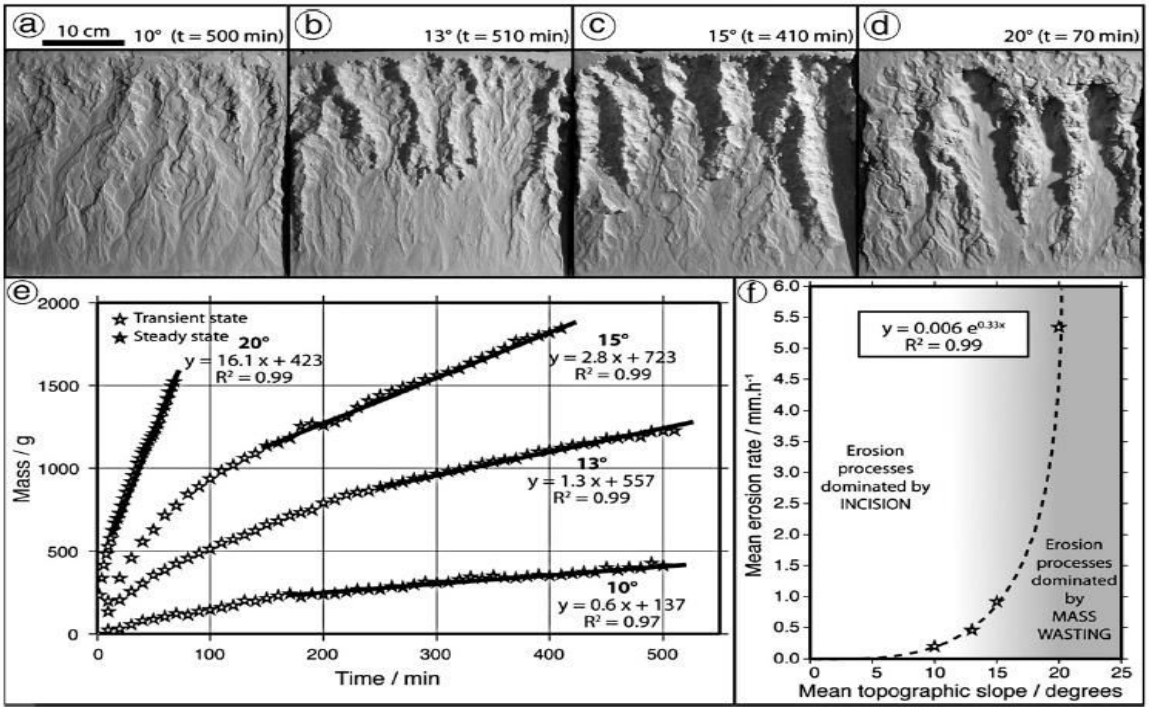

Figure. 10. Estimation of mean erosion rate for MatIV atvarious initial slopes. a-d) Pictures of final stage morphology at (a) 10° initial slope, (b) 13°, (c) 15° and (d) 20°. Note that experimental duration is different between each test. Morphology in each picture displays 4 to 5 straight drainage basins with associated channel valley and crest. (e) Plots of mass of eroded particles versus time for each surface slope. A first exponential phase (open symbols) and a second seemingly linear phase (full gray symbols) can be distinguished for each curve, and may correspond respectively to a transitory and a stationary phase of erosion flux. Each linear regression for the stationary phase has been interpreted as indicative of mean erosion rate for MatIV, depending on initial slope. (f) Plot of mean erosion rates as a function of slope for MatIV. The exponential fit suggests a threshold slope between 15 and 20° where erosion processes change from an incision-dominated regime to a mass-wasting-dominated regime.

3.6.3. Erosion properties for MatIV

The previous deformation and erosion tests have demonstrated that MatIV is an experimental material that accounts for first order deformation characteristics of the continental crust (faults, thrust slices) and first order morphology of mountainous relief (valley, channel, crest and hillslopes). In the following, it was characterized more precisely its erosion properties, namely the evolution of mean erosion rates as a function of initial slope and its corresponding erosion law.

3.6.3.1. Mean erosion rates.

It is analyzed that the evolution of MatIV mean erosion rates for increasing initial slopes under a constant precipitation rate of25±1 mm/h (Fig. 10). Initial slopes were 10, 13, 15 and 20 ±0.1°. the final stage morphology was presented for each experiment (Fig. 10a-d) and the evolution of erosion fluxes for each slope (Fig. 10e). Each curve can be broadly divided into two successive domains. The first domain starts at the beginning (t = 0) and stops at t= 150-250 min for slopes 10, 13 and 15° and t= 10-15 min for 20°. This portion has a broad exponential evolution that could be tentatively interpreted as a transitory phase of the drainage network evolution. Note that it does not correspond to the connectivity of the drainage network (Lague et al., 2003) as full connectivity is achieved very rapidly (after 5 to 10 min of experiment). In the following, it is not analyzed that this initial part of the curve but focus on the second phase. This second phase lasts till the end of the experiment and is characterized by a nearly linear evolution of the sediment mass with time. It is presumed that this linear phase would tend to flatten and reach a near zero mass flux after several tens of hours or days (Schumm and Rea, 1995). Nonetheless, this constant sediment flux indicates that topography is transferring material at a steady rate. It is evaluated sediment yields (Q) as a function of

slope for these steady phases by using root mean-square correlations. It gives sediment yields around 0.6±0.1 g/min for 10°, 1.3±0.1 g/min for 13°,2.8 ±0.1 g/min for 15° and 16.1 ±0.1 g/min for 20° (Fig. 10e). It indicates, as expected, that the steeper the initial slope, the quicker the model exports material.

Solid load measurements at a river outlet can be interpreted in terms of upstream mean denudation rates (Summerfield and Hulton, 1994). This approach was followed and calculated a minimum erosion rate for each steady curve. Given the mean particle density of MatIV ($\rho_{\mathrm{Part-MatIV}} >= 2.22\ \mathrm{g/cm^3}$), porosity ($\theta_{\mathrm{MatIV}} = 34\%$) and the total area of the box (A_{total}= 1242 $\mathrm{cm^2}$) mean erosion rate (E) for each slopes can be calculated (Eq. (6)): and it was calculated that the erosion law parameters that best fit the experimental dataset.

$$E = \frac{Q}{\langle \rho_{\mathrm{Part\ MatIV}} \rangle . (1-\theta_{\mathrm{MatIV}}) . A_{total}} \tag{6}$$

Results give mean erosion rate around 0.20± 0.01 mm/h at 10°, 0.43 ± 0.01 mm/h at 13°, 0.92 ± 0.01 mm/h at 15° and 5.30 ± 0.01 mm/ h at 20°. Plotted in a mean erosion rate versus slope diagram, the dataset appears strongly non linear and follows an exponential trend (Fig. 10f). The sharp increase in erosion rate between 15 and 20° indicates a clear change in the dominant erosion processes shaping MatIV. It is incision processes below and mass wasting processes above. Interestingly, this experimental trend of erosion rates as a function of mean slopes is comparable to natural datasets obtained in different mountain belts (Montgomery and Brandon, 2002).

3.6.3.2. Erosion law.

Erosion law equations were investigated to compare the transport dynamics in the model and in nature. With this aim, it is analyzed the sediment yield curves obtained for each slope and was calculated the erosion law parameters that best fit the experimental dataset.

Channelized processes, and particularly fluvial processes, are often modelled by considering that sediment transport and incision are controlled by the shear stress acting on the riverbed (Howard and Kerby, 1983). The so-called "stream power" model assumes that incision can be linked to upstream drainage area A and local slope S (Howard et al., 1994; Stock and Montgomery, 1999; Tucker and Whipple, 2002) (Eq. (7)):\

$$\frac{dz}{dt} = kA^m . S^n \tag{7}$$

where m and n are positive exponents and k is a dimensional coefficient of erosion. In addition, Hack's law links the drainage area A to the stream length x downstream of the drainage divide (Hack, 1957) (Eq. (8)):

$$A = k_H . \chi^h \tag{8}$$

where k_H is a dimensional constant and h is the reciprocal of the Hack's exponent. Accordingly, Eq. (7) can be rewritten (Eq. (9)):

$$\frac{dz}{dt} = k . \chi^{hm} . S^n \tag{9}$$

where $\mathrm{K = k.k_h^m}$ is a parameter accounting for hydraulic roughness and bed sediment characteristics. It depends on lithology, climateand sediment load (Stock and Montgomery, 1999; Whipple and Tucker,1999). Eq. (9) allows modeling the evolution of a longitudinal profile

Table 2: Best fitting parameters of the stream power laws for the different initial slope (α). rms values in bold reflects experiments where the power law equation accounts for the sediment flux evolution, whereas rms in italic reflects a case where the power law equation is not adapted to account for the experimental data.

α	K	HM	n	rms
10	$4.79.10^{-8}$	3.0	1.0	**0.036**
13	$4.79.10^{-8}$	3.0	1.0	**0.020**
15	$4.79.10^{-8}$	3.0	1.0	**0.034**
20	$4.79.10^{-8}$	3.0	1.0	*0.091*

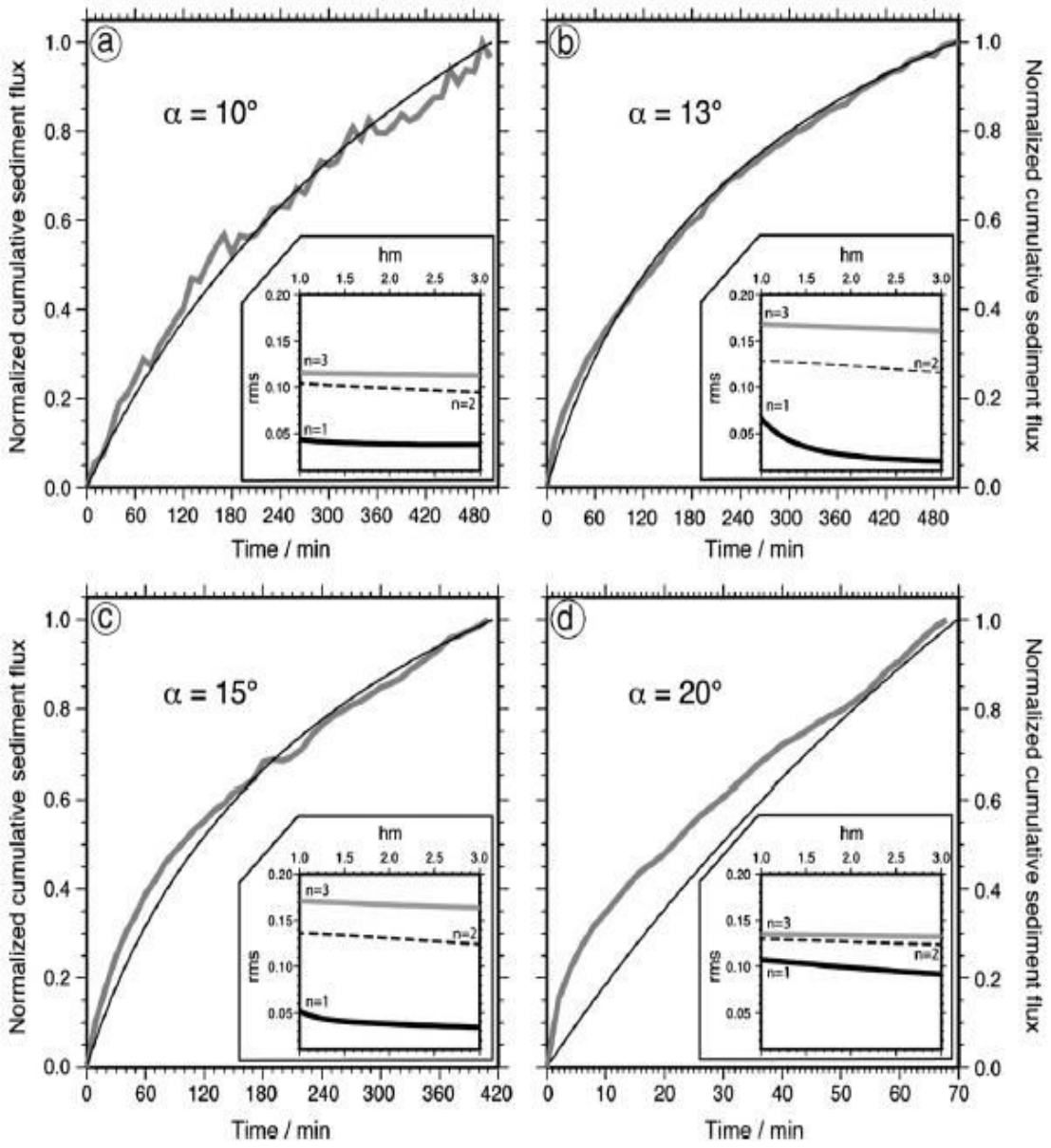

Figure. 11. Comparison between experimental sediment flux (thick gray lines) for each slope and the numerical simulation of stream power erosion law (thin black lines) for different initial slopes α. (a) α = 10°; (b) α = 13°; (c) α = 15°; and (d) α = 20°. Insets give the rms values versus hm values, for different exponents n. Best fitting exponents are for lower rms values, that is hm = 3.0 and n = 1 in all cases. The represented numerical simulations of the experimental sediment flux are the best-fit model obtained with the best fitting exponents hm and n. The fit is good for 10, 13 and 15° slope but not for 20° (high rms value). The modeled stream power erosion law does not apply to this slope as hillslope processes dominate over incision processes.

(dz/dt) within the experimental box by calculating the elevation difference due to incision for each point representing the river profile. This 1D longitudinal profile was then integrated over the width of the box (i.e. 0.347 m) in order to calculate the whole sedimentary flux exported at the static basin outlet. This calculated sediment budget was compared to the experimental measurements, which constrain the likely exponents of the erosion law. By looking for the best fitting equation with 3 unknowns (K, hm and n), hm and n was forced to vary by increments of 0.1 between 1 and 3 and was optimized K to minimize the sum of the differences between the model and the measurements (Stock and Montgomery, 1999). From the collection of couples of (hm, n) and best value of K, a least-square algorithm was then used to calculate the best fitting stream power law parameters.

Results show that the best fitting parameters K, hm and n in the experiments are similar for all the initial slopes of the box and therefore independent on this parameter (see Table 2, and insets on Fig. 11). It makes sense as the experiments are carried out in the same conditions of uniform lithology and precipitation where K, hm and n are supposed to be constant (Whipple and Tucker, 1999). Given these parameters, the best fitting models compare well with the evolution of sediment flux with time in experiments (Fig. 11). The modeled sediment flux is consistent with experimental data for slopes lower than or equal to 15° (Fig. 11a, band c), but fails to reproduce the sediment evolution for 20° initial slope (see rms in Table 2 three times higher than for $\alpha < 15°$ and Fig. 11d). This probably reflects that the dominant erosion process in this experiment (mass wasting and land sliding) is not well accounted by the stream power law. In particular, the equation used is not appropriate to reproduce the very important sediment flux measured in the first 10 min. Best fitting slope exponent (n) of stream power law is equal to 1.0 in the experiments. This value is within the range of typical values derived from field data (Howard and Kerby, 1983; Stock and Montgomery, 1999; Tarboton et al., 1989) and theoretical considerations (Tucker and Whipple, 2002; Whipple and Tucker, 1999). Exponent hm can be considered as relatively high (best fitting value = 3.0; Table 2). Indeed, in nature reciprocal Hack's exponent h ranges between 0.93 and 2.12 (Hack, 1957; Rigon et al., 1996; Stock and Montgomery, 1999) and exponent m (about 0.1 to0.5) (Snyderetal.,2000; Stockand Montgomery, 1999) would lead to an exponent hm between 0.9 and 1.1. Given the natural reciprocal Hack's exponent h, exponent m in the experiment would be between 1.42 and 3.20. Therefore, the m/n ratio in experiments (m/n= 3) is out of range of typical values in nature (between 0.35 and 0.6) (Whipple and Tucker, 1999). However, the agreement for exponent n between the model and nature suggests that the dominant erosion process in the experiment catch the essence of dominant erosion processes in natural watersheds. In addition, exponent m characterizes a discharge-drainage area relationship that is weighted by the importance of discharge on incision. In the experiments, precipitation is held constant through time whereas rainfall is non-uniform in space and time in natural catchments, notably during a high precipitation episode where the transport capacity can be strongly increased. Thus, the uniform distribution of precipitation in the experiments likely explains the high values of exponent. Finally, from a theoretical approach, Whipple and Tucker (1999) have demonstrated that the sensitivity of river profiles to varying lithology, climate or uplift is strongly related to the slope exponent n. In the experiments, this exponent scales like natural watersheds, which indicates that the modeling is appropriate to catch the fundamental aspect of landscape evolution.

4. Discussion

4.1. Example of application

MatIV was tested in a typical experiment of piedmont deformation and erosion to study how it deforms and erodes. The experimental setup presented was used in a previous complementary article (Graveleau and Dominguez, 2008) (Fig. 12A). Deformation processes was triggered by pulling a basal film covered by MatIV beneath a rigid backstop and surface processes were activated by sprinkling water micro-droplets over the model surface. The example described in Fig. 12Billustrates the final stage of an experiment that lasted 12 h at constant rainfall (25 ± 5 mm/h) and convergence rates (30 mm/h).

Bulk shortening was 23 cm. Given a length ratio of $1\text{-}2.10^{-5}$ (1 cm = 500-1000 m; see next section), the model focused on the upper 10-15 km of the continental crust. From bottom to top, initial stage was composed of three main layers (Fig. 12A): (1) a 6cm thick deep layer made of a GM and PVC mixture (MatII) and representing a potential deep low-strength rheology; (2) a 10 cm thick MatIV layer tapering outward and representing the continental basement; (3) a 6 cm thick stratified body composed of alternating layers of MatIV (0.7 cm) and GM (0.3 cm) tapering to the right and modeling the pre-existing stratified foreland basin.

Fig. 12B.a presents an oblique view of the model at final stage. Two close up pictures of the surface morphology (Fig. 12B.b) and the internal structures (Fig. 12B.c) are provided to detail how the selected material eroded and deformed respectively. Concerning the deformation style, the model

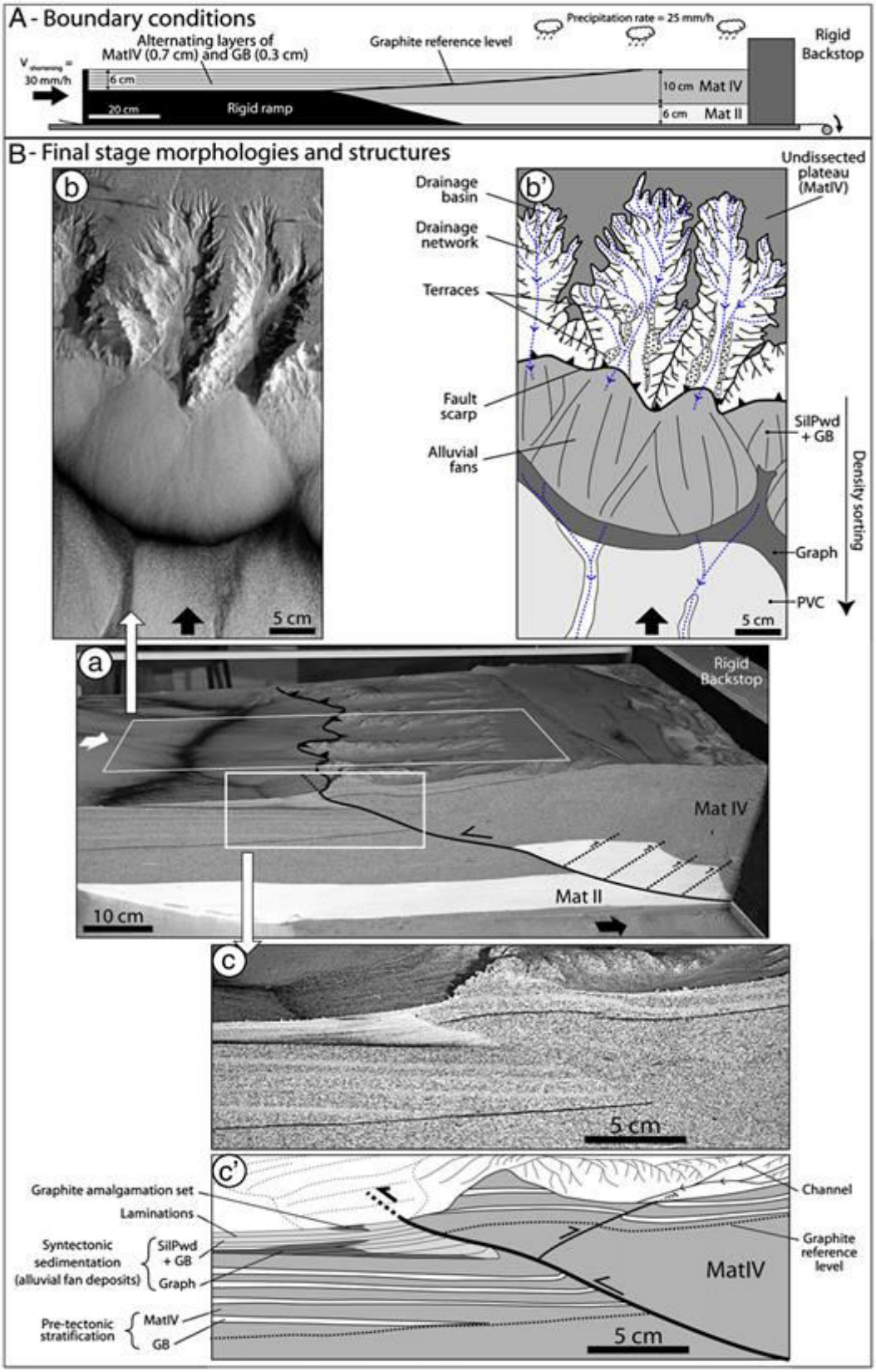

Figure. 12. Application of MatIV in an orogenic wedge setting. A) Boundary conditions of the experimental set-up. B) Final stage morphologies and structures. (a) Oblique view ofthe cross-sectioned model displaying both plan views of the surface and cross-sections close-up. b and b') Digital picture and schematic diagram of the experimental morphology. c and c') Digital picture and schematic diagram of the fault structure near the surface.

is affected by a main thrust dipping 20° toward the rigid backstop. In plan view, the active thrust scarp is underlined by the juxtaposition of two contrasted materials: the dark gray original MatIV in the hanging wall, and a bright gray syntectonic material in the footwall (Fig. 12B.b). In cross-section, a close view of the fault geometry indicates that the thickness of the shear zone is relatively thin (about 1 mm) (Fig. 12B.c). A minor backthrust is associated to the main thrust and developed in response to a change in the fault plane geometry near the surface. Finally, the hanging wall is slightly folded as underlined by GM bent layers. This folding is due to GM layers, which weakened the bulk strength of the MatIV sequence and promoted flexural slip.

The experimental topography displays a wide range of morphological features, which range in size from few millimeters to several centimeters. The deformation front is marked by a 3-5 cm high cumulative relief above the flat undeformed lowland and it is dissected by several adjacent drainage basins separated by straight crestlines (Fig. 12B.b and b'). These basins are elongated perpendicular to the fault trend and measure 20-25 cm long and 8-10 cm wide. Drainage basin surfaces are in the range of 50 to 200 cm^2 and display drainage networks with two to three stream orders according to Strahler classification (Strahler, 1957). Due to the flat initial topographic surface, drainage basins mainly grow by headward erosion and catchment widening. Channels are 2-3 cm wide in downstream domains but they rapidly narrow upstreamward. In the valley, strath and alluvial terraces have been formed in response to simultaneous topographic uplift and channel incision phases. Their differences in height rarely exceed 1 or 2 mm and their lengths range from a few centimeters to 7-10 cm. These dimensions will be used in Section 4.3.1 to evaluate a mean geometric scaling factor.

Finally, concerning syntectonic sedimentation, fan-shaped sedimentary bodies rest at drainage basin outlets, downstream to the active thrust (Fig. 12B.b). They correspond to alluvial fan sediments accumulated at the bottom of the uplifting and eroding relief. Their surface is around 150-180 cm^2 in average and displays contrasted sediment colors according to the distance from the active front (Fig. 12B.b'). Close to the fault, "proximal" facies are composed of silica (either GM or SilPwd). Mid-distance facies are composed of black Graphite particles that lay at about 15-17 cm from the fan apex. Distal facies correspond to white particles of PVC that generally spread on a large surface. This sorting results from the density and shape contrast between MatIV particles. GM and SilPwd have the heaviest particle density (around 2.5-2.65; Table 1) and therefore have the shortest characteristic transport distance. Graphite and PVC, with particle density around 2.25 and 1.38 respectively (Table 1) and planar or globular shapes, are lighter and are transported farther. In cross-sectional view, internal domains are thrusted over syntectonic deposits that taper toward the undeformed lowland (Fig. 12B.c). Their thickness below the active thrust reaches about 2 cm. Sediments are finely stratified and display downlap structures that indicate foreland progradation. "Proximal" and "distal" sediments can be distinguished according to their color (Fig. 12B.c'). Note that a few PVC particles are preserved in this cross-section because they travel farther toward the free boundary conditions in the lowland. Additional experiments have shown that PVC powder could be preserved in syntectonic deposits of piggy-back basins and indented with graphite and silica (Graveleau et al., 2008). Finally, graphite powder delineates the unconformity between ante-tectonic stratification and syntectonic sediments and records the lateral amalgamation of alluvial fans deposits (Fig. 12B.c').

4.2. Modeling deformation and surface processes

The experimental tests show that pure granular materials such as GM, PVC or SilPwd do not fully satisfy the experimental and physical specifications. GM and PVC present a satisfying deformational style but develop non-realistic landscape morphology dominated by mass wasting processes. SilPwd has a very brittle and unrealistic deformation style to model active piedmont tectonics but it develops a detailed morphology mainly shaped by channelized processes. Accordingly, mixtures composed of these three components was tested and a material (MatIV) was selected whose composition (40% of GM, 40% of SilPwd, 18% of PVC and 2% of Graph) takes advantages of each pure component. MatIV deformation style is controlled by GM and PVC, whereas SilPwd is mainly responsible for the realistic sharpness of morphological details. The observation of internal structures in experiments shows that MatIV generates thrust faults comparable to natural orogenic thrusts (Fig. 12B). Continuous observation of model evolution shows that MatIV erodes dominantly by stream incision processes, which control drainage basin dynamics (Fig. 12B), and also by intermittent landslides on the steepest hillslopes. These landslides may explain why overhangs

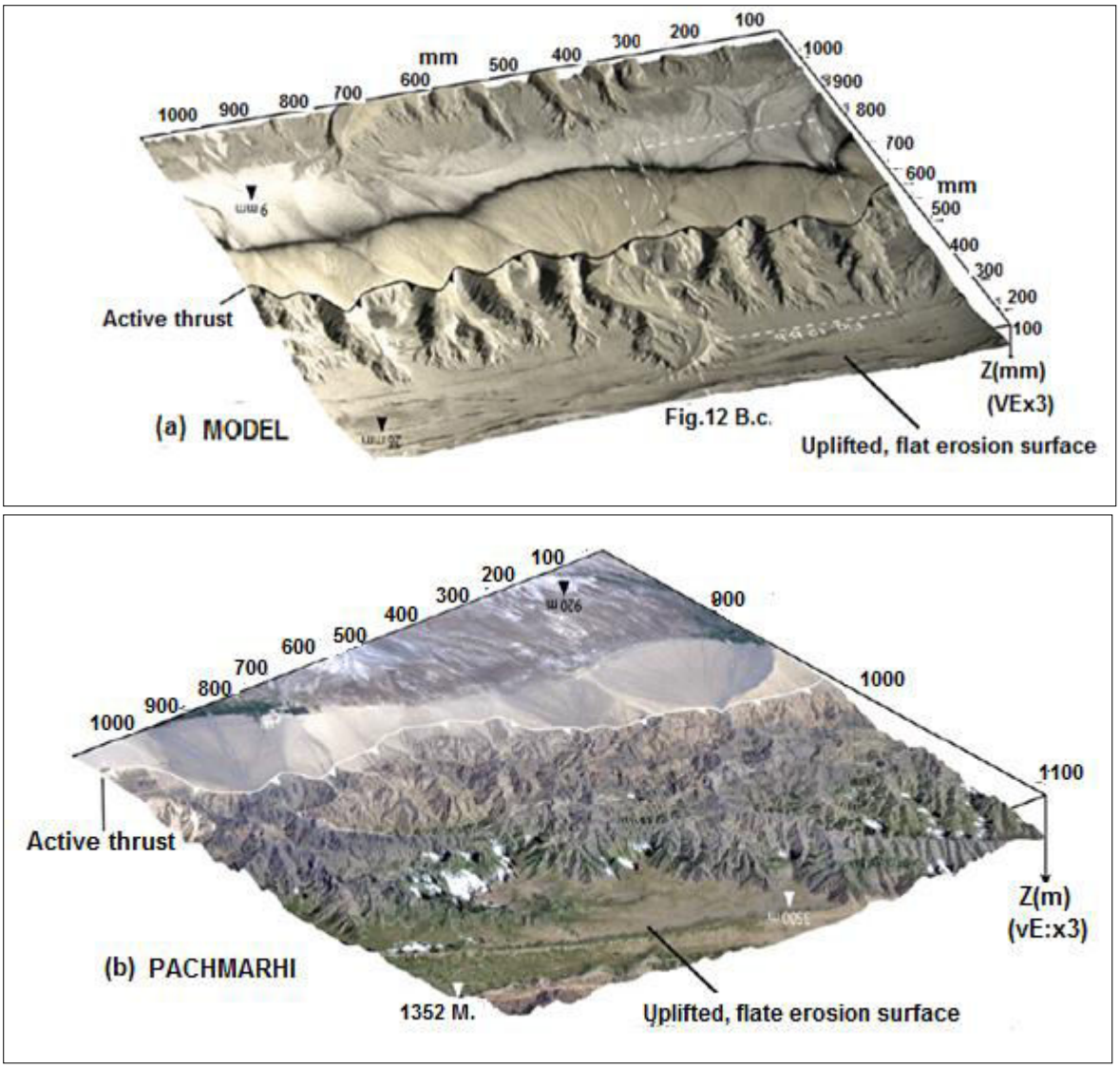

Figure. 13. 3D morphological comparison between model (a) and natural piedmont (b). For the model, a digital picture is draped over an experimental DEM performed with a laser interferometer device. The natural example is issued from the Pachmarhi northern piedmont. A Landsat satellite image is IRS-IC PAN STEREO IMAGELandsat.org.

along channels are scarce and why sharp crests can form between adjacent watersheds. Finally, the composition of MatIV based on wide granulometric distribution and contrasted color and density of particles facilitates the analysis of alluvial fan evolution. At the surface of experiments, they display detailed morphological features (terraces, distributary channels) and proximal and distal facies due to various characteristic transport distances of particles. In cross-section, the depositional evolution is recorded by finely stratified layers, whose geometry (downlap, cutoff, proximal and distal sets) records the sedimentary evolution of the piedmont and its morphological evolution.

4.3. Scaling

It was compared that experiment results with the morphology and tectonics of a natural mountain belt to evaluate the geometric, dynamic and kinematic scaling and better constrain the comparison between model and nature (Fig. 13). The Pachmarhi (India) was used as a natural counterpart to this models because it displays impressive morphological and tectonic markers that remarkably illustrate the interactions between tectonics, erosion and sedimentation. The Pachmarhi is an active intra-continental mountain belt presently characterized by slow convergence rates (10-20 mm/yr) and mansoon type of climatic conditions (mean precipitation rate above1, 000 mm/yr) . One

have to keep in mind that this comparisons are necessarily limited by the constancy of erosion boundary conditions in model whereas they have changed on the field due to cyclic climatic regimes ..

4.3.1. Geometric scaling

It was first analyzed non-dimensional geometric characteristics for drainage basin (relief ratio) and alluvial fan shape (surface slope) to assess the geometric similarity between experiment and nature. Theoretically, such values should be equal in nature and models. In the experiment, the topography develops with relief ratio around 30-58% (16-30°) and alluvial fans form with surface slope around 5-9% (3-5°; Table 4). In the Pachmarhi, relief ratio of several river catchments are intherange of 7-17% (4.0-9.7°) and associated fan slopes are around 2.7-5.1% (1.5-2.9°) . Consequently, slopes in model and nature are in the same range for alluvial fans but not for to-pography. The agreement for alluvial fan slopes suggests that similar transport-deposition processes (likely debris flow) govern fan dynamics. The difference in relief ratio could correspond to a transitory phase of the topographic evolution or a low erodibility of MatIV. This low erodibility would stymie mass wasting processes on hillslopes and it would limit channel incision capacity. Such limitation is illustrated by the tilted downstream zones observed in relaxation erosion tests (Figs. 9eand 10), which likely indicate the presence of a significant erosion threshold for incision and transport.

To estimate a mean geometric scaling factor (L*) between model and nature, a range of values was calculated from the measured properties of density and cohesion of MatIV and from the similar properties for natural rocks (Schellart, 2000) (Table 3). Based on the dynamic scaling Eq. (1) (see next section for details), results indicates that L* is in the range of $2.0\ 10^{-4}$-$1.0\ 10^{-5}$, that is, 1 cm in experiment equals 50-1000 m in nature. To verify this range, it was estimated L* with another independent method. The sizes of several morphological features in the experiment was compared and in the Pachmarhi (Fig. 13) and summarized the results in Table 4. It is not a trivial issue as drainage basins and alluvial fans grow during the experiment. However, morphologic features in the model display generally homogeneous sizes from one experiment to the other because the set-up frame and boundary conditions (shortening rates in the range of 30-40 mm/h) are similar and because experiments are performed using a constant rainfall (around 25-30 mm/h). It was compared that the dimensions of catchments, channels, alluvial fans and terraces (height, length, width) in models and from the Pachmarhi morphometric measurements carried out from government of India topo sheet 55-J-7 and satellite image. Results indicate that geometric scaling factors are relatively similar for piedmont relief (1 cm = 600-1500 m) and terrace height (1 cm= 250-1000 m). Horizontal dimensions have slightly different scaling factors for valley width (1 cm = 50-1200 m), terrace length (1 cm = 10-500m), drainage basin width (1 cm = 500-1875 m) or valley length (1 cm = 600-2000 m).

These discrepancies illustrate how difficult it is to use a single feature to compare nature to model. It may result from some incomplete scaling, particularly dynamic scaling (see next section), that would induce improperly scaled erosion and transport processes. However, the two scaling techniques provide an average geometric scaling factor in the same range of $1\text{-}2.10^{-5}$; that is 1 cm in experiment equals 500-1000 m in nature. This ratio is obviously a crude value that results from several approximations but its consistency over several methods and through various experiments allows useful means for comparing models to natural morphologies and to analyze the evolution of mor-photectonic features.

4.3.2. Dynamic scaling

Dynamic scaling in the experiment can be investigated from a tectonic and hydraulic point of view. Concerning tectonics, Eq. (1) governs the dynamic scaling and typical ranges of values of parameters are summarized in Table 3. Gravity in model and nature are similar (so g*= 1) and a mean length ratio has been proposed above ($L^* = 1\text{-}2.10^{-5}$). Considering the bulk density of MatIV ($\mathbf{p}_{MatIV}$=1600 kg.m^{-3}) and natural rocks (between 2000 kg.m^{-3} for sandstone and 2800 kg.m^{-3} for granite), the density ratio $\boldsymbol{\rho}^*$ (between 0.57 and 0.80) and cohesion in natural rocks (between 10^7 Pa for sandstone or granite and 10^8 Pa for marble and limestone) (Schellart, 2000), cohesion in the model should be in the range of 100-1600 Pa to satisfy Eq. (1).With a measured extrapolated cohesion of 750-1200 Pa in stable and peak friction conditions (Table 1), MatIV lies in a reasonable range of

Table 3: Characteristic values of gravity, length, density, angle of internal friction and cohesion in nature and experiment. Density of 2000 kg.m^{-3} is for sandstone whereas 2800 kg.m^{-3} is for Basalt. Cohesion of 10^7 Pa is for sandstone .

	Gravity	Length		Density		Angle of internal	Cohesion	
	(m.s^{-2})	(m)		(kg.m^{-3})		(°)	(Pa)	
		Min	Max	Min	Max		Min	Max
Nature	9.81	50	1000	2 000	2800	25-45	10^7	10^8
Experiment	9.81	0.01		1600		40-48	1200	750
Model to nature ratio	1	2.0 10^{-04}	1.0 10^{-05}	0.80	0.57	_	1.2 10^{-4}	7.5 10^{-6}

Table 4: Comparison between morphological dimensions of several features in experiment and on the field. Field data are extracted from catchments in the south-eastern piedmont of the Pachmarhi mountain range (Dongre, 1999,2011).

		Experiment (cm)	Pachmarhi (m)	Scaling factor	
				L*	1 cm (model) =... m (nature)
Vertical	Piedmont relief	3-5	3000-4500	6.7 10^{-6}-1.7 10^{-5}	600-1500
	Terrace height	0.1-0.2	50-150	4.0 10^{-5}-6.7 10^{-5}	250-1500
Horizontal	Drainage basin length	20-25	15,000-30,000	6.7 10^{-6}-1.7 10^{-5}	600-1500
	Drainage basin width	8-10	5000-15,000	5.3 10^{-6}-2.0 10^{-5}	500-1875
	Valley length	20-25	15,000-40,000	5.0 10^{-6}-1.7 10^{-5}	600-2000
	Valley width	0.5-2	100-600	8.0 10^{-6}-2.0 10^{-4}	50-1200
	Alluvial fan radius	10-20	8000-12,000	8.3 10^{-6}-2.5 10^{-5}	400-1200
	Terrace length	1-10	100-5000	2.0 10^{-6}-10^{-3}	10-5000
	Terrace width	0.2-1	100-500	4.10^{-6}-10^{-4}	100-2500
Geometrical ratio	Relief ratio	16-30°	4.0-9.7°		
	Alluvial fan slope	3-5°	1.5-2.9°		

values for modeling the brittle upper crust. Moreover, the angle of internal friction (40-48°) is also compatible with natural rock values (i.e., 25-45°) (Schellart, 2000).

Concerning hydraulic processes, previous experimental works was followed and calculated Froude and Reynolds numbers to investigate the dynamic scaling of the erosion processes. In experiments, flow depth ranges from 5.10^{-4} m to 10^{-3} m and velocity ranges from a few mm/s to a few cm/s (Table 5). Using a kinematic viscosity of 10^{-6} Pa.s (pure water), these values imply laminar (0.5<Re< 100) and subcritical fluvial flow (0.01 <Fr< 1), which are classic values measured in "microscale river" experiments (Malverti et al., 2008). On the field, hydraulic measurements along mountainous rivers generally characterize subcritical-turbulent or supercritical-turbulent flows (Mount, 1995). For instance, the Denwa river in northern Pachmarhi indicates average turbulent Reynolds number of 370 000± 280 000 and average subcritical Froude number of 0.44±0.18 . Thus, Froude numbers fit between model and nature but not Reynolds numbers. This discrepancy is due to the improper use of water as a flowing liquid in model (Paola et al., 2009; Peakall et al., 1996) but it is not a limiting factor. Indeed, channels in experiment and nature respond to the same balance of forces that promotes gravitational forces over inertial and viscous forces (Niemann and Hasbargen, 2005). In addition, relaxing Reynolds number is allowed since turbulent and laminar channels are governed by identical dimensionless equations and therefore follow the same dynamics (Malverti et al., 2008).

4.3.3. Kinematic scaling

Kinematic scaling is generally not a problem in purely frictional sandbox models since dry sand rheology does not depend on strain rate (Horsfield, 1977). As mentioned earlier (see Section 2.2), kinematic scaling in experimental modeling of landscape dynamics is much more problematic to achieve because numerous time scales for erosion-transport processes coexist (Lague et al., 2003;

Schumm et al., 1987). However, the idea to evaluate a mean temporal scaling factor at the scale of the whole model was challenged by comparing first order transfer fluxes between model and nature. For that, the analysis on comparing mean erosion rates was based.

To estimate average erosion rates for MatIV, it was used that the results from tectonically inactive experiments performed with initial slopes ranging from 10 to 15° (see Section 3.6.3.1). For these slopes, erosion rates are in the order of 0.1-1 mm/h (Fig. 10f). In natural mountain belts, mean erosion rates vary significantly depending on the range (Ahnert, 1970; Montgomery and Brandon, 2002; Pinet and Souriau, 1988), the measurement methodology and the considered time scale (Kirchner et al., 2001). However, if it was considered that only average estimations in tectonically inactive areas, mean erosion rates in nature are in the order of 0.01 to 0.2 mm/year (Montgomery and Brandon, 2002). Note that it is almost one to two orders of magnitude lower than values in tectonically active convergent areas (Montgomery and Brandon, 2002). Given the geometric scaling ratio between model and nature presented above ($L^* = 1\text{-}2.10^{-5}$), it can be calculated a mean temporal scaling factor between the relaxation experiments and natural tectonically inactive areas. The full range of time ratio t* is then between $1.1\ 10^{-11}$-$4.6\ 10^{-9}$, which corresponds to 1s=7-2800 years. It can be reasonably restricted this range by comparing the slowest values from the experiment with the slowest in nature, and similarly with the highest. Then, the temporal scaling factor range shrinks to $1.1\text{-}4.6\ 10^{-10}$ that is 1 s = 69-280 years. By arbitrary averaging this result, it was proposed that the presented material (MatIV) erodes with a mean temporal scaling factor around 1s=100-300 years. It is stressed that this proposition must be considered with caution because of the simplifications on both experimental and natural measurements. It was recognized that all the geomorphic rates in the model (for instance, incision rate or knickpoint retreat rate) are probably not properly downscaled to their natural counterparts according to this time ratio. It is particularly not valid at a very local scale due to improper dynamic scaling of erodibility or fluvial processes, as noted in the previous section. That said, the calibration gives a very interesting order of magnitude estimate to catch the analogy between model and nature. This kinematic scaling should benefit from future work performed with tectonically active conditions by monitoring erosion rates at the scale of drainage basins in the model (as on Fig. 12) and to compare these values with their counterparts in natural landscapes (the Himalaya, the Olympic Mountains, Satpura Mountain, Pachmarhi, etc.). It was thought that the time ratio should not vary significantly because higher erosion rates in model will be compared to higher erosion rates in nature. First results obtained on comparisons between morphotectonic experiments of triangular facets and natural extensional landforms confirm this suggestion since time and spatial scaling factors are similar to this work.

4.4. Saturation ratio and compaction

Saturation ratio is a key parameter for the experimental material developed because it controls both its mechanical behavior and its erosional properties. Basically, it was observed that a major change in material rheology occurs between the first top millimeters of the material and at depth. Indeed, when MatIV is submitted to standard experimental conditions (continuous rainfall), the first half-centimeter of the material is mechanically very soft (likely low internal friction and medium cohesion). Consequently, all the typical experimental morphologies shown in Fig. 12 are not rigid features but rather very soft landforms that can spread easily under a gentle finger's touch. This indicates that MatIV is a thixotropic material likely close to water saturation ratio near the surface. However, the occurrence of centimeter high topography and even overhangs on hillslopes suggest that these upper centimeters are actually not totally saturated but still have enough capillary cohesion to sustain relief. If the material were fully saturated, crests, ridges and overhangs could not form and model morphology would be very smooth. Additionally, MatIV's moderate permeability (see Section 3.4) implies that rainfall infiltrates slightly on hillslopes (seepage fluxes are certainly very low). This may increase local saturation ratio, influence slope stability and trigger mass wasting (landslides). In channel networks, similar infiltration of runoff probably occurs but incision is related to the shear stress of the fluid/particles flow applied at the boundary layer. The basal shear stress is then able to overcome the threshold for detachment and transport of particles (Howard, 1994) and, like in nature, induces progressive erosion of the river bed. Rapid variations of incision rate allow terrace formation and affects the hillslope base-level, which controls potential mass wasting events (Burbank et al., 1996).

At depth, MatIV shows a significant downward hardening. It is likely related to a change in porosity, saturation ratio and density due to lithostatic pressure and compaction. It has not been able to measure this strength evolution with depth but the first estimations suggest that, at the surface, internal friction would be very low whereas cohesion would be on the order of several hundreds of Pascal. At depth, internal friction would be close to values measured in Section 3.5.1.2 and cohesion in the order of several thousands of Pascal. It is presumed that both these friction and cohesive properties should stabilize rapidly with depth, maybe 1 cm below the surface. This feature is not necessarily a limiting factor since a similar strength hardening with depth is classically considered for the brittle upper crust (Byerlee, 1978). In addition, the measurements of mean frictional properties suggest that MatIV is reasonably well scaled to natural rock basement but a little too strong compared to sedimentary rocks. To overcome this limitation, MatIV is usually interstratified with GM layers in the outward domains to weaken the strength of the material pile (see Fig. 12) and more closely match the rheology of foreland sedimentary fill.

5. Conclusion

A new experimental approach was developed to model simultaneous deformation and erosion-transport-sedimentation processes in a mountain range piedmont. Because common materials for tectonic and geomorphic experiments were not suitable for this approach, it was tested various granular materials in water-saturated conditions. These included glass microbeads "GM", silica powder "SilPwd", plastic powder "PVC" and graphite "Graph". If used pure, GM, SilPwd and PVC materials did not display suitable deformation styles and erosion morphology so a mixture, called MatIV was developed, made up with 40% GM, 40% SilPwd, 18% PVC and 2% Graph (percentage in weight). This material represents an interesting compromise because it correctly satisfies the following physical criteria for erosion and deformation inspired from nature:

1. From a tectonic point of view, MatIV satisfies Mohr-Coulomb failure criterion, localizes deformation along shear zones (faults) and presents reasonably downscaled frictional properties.
2. From a morphological point of view, MatIV erodes by channelized processes (fluvial-like incision) and hillslope processes (mass landslides) that reproduce morphogenetic evolution of natural mountains. It generates topography with morphological features like drainage basins, channel networks, crests and terraces. Its erosional properties have been investigated in relaxation experiments and measurements of erosion fluxes allowed evaluating exponents of a stream power erosion law. The erosion parameters scale reasonably well with natural catchments, which indicate that erosion-transport processes with MatIV are comparable to natural mass transfer laws in real drainage basins.
3. From a sedimentologic point of view, transport and deposition processes of MatIV generate fan shape sedimentary objects. These fans present detailed features in plan view (active and inactive channels) and cross-section (stratification, segregation of distal and proximal deposits) that compare well with the dynamic and geometric record of natural alluvial deposits.

In conclusion, new experimental material MatIV developed in this study appears very promising and suitable to investigate new geological issues concerned with interactions between deformation and surface processes in various tectonic and climatic settings.

References

Adam, J., Urai, J., Wieneke, B., Oncken, O., Pfeiffer, K., Kukowski, N., Lohrmann, J., Hoth, S., van der Zee, W., Schmatz, J., 2005. Shear localisation and strain distribution during tectonic faulting—new insights From granular flow experiments and high-resolution optical image correlation techniques. Journal of Structural Geology 27 (2), 283-301.

Ahnert, F., 1970. Functional relationships between denudation, relief, and uplift in large mid-latitude drainage basins. American Journal of Science 268 (3), 243-263.

Babault, J., Bonnet, S., Crave, A., Van Den Driessche, J., 2005. Influence of piedmont sedimentation on erosion dynamics of an uplifting landscape: an experimental approach. Geology 33 (4), 301-304.

Baby, P., Colletta, B., Zubieta, D., 1995. Etude geometrique et experimentale d'un bassin transporte: exemple du synclinorium de l'Alto Beni (Andes centrales). Bulletin de la Societe Geologique de France 166 (6), 797-811.

Bigi, A., Hasbargen, L., Montanari, A., Paola, C., 2006. Knickpoints and hillslope failures: interactions in a steady state experimental landscape. In: Willett, S.D., Hovius, N., Brandon, M.T., Fisher, D.M. (Eds.), Tectonics, Climate, and Landscape Evolution: GSA Special Paper, pp. 295-308.
Bonnet, S., 2009. Shrinking and splitting of drainage basins in orogenic landscapes from the migration of the main drainage divide. Nature Geoscience 2 (11), 766-771.
Bonnet, S., Crave, A., 2003. Landscape response to climate change: insights from experimental modeling and implications for tectonic versus climatic uplift of topography. Geology 31 (2), 123-136.
Bonnet, S., Crave, A., 2006. Macroscale dynamics of experimental reliefs. In: Buiter, S.J.H., Schreurs, G. (Eds.), Analogue and Numerical Modelling of Crustal-Scale Processes. London, Special Publications, London, Geological Society, pp. 327-339.
Bonnet, C., Malavieille, J., Mosar, J., 2007. Interactions between tectonics, erosion, and sedimentation during the recent evolution of the Alpine orogen: analogue modeling insights. Tectonics 26 (TC6016).
Bonnet, C., Malavieille, J., Mosar, J., 2008. Surface processes versus kinematics of thrust belts: impact on rates of erosion, sedimentation, and exhumation—insights from analogue models. Bulletin de la Societe Geologique de France 179 (3), 179-192.
Bryan, R.B., Hawke, R.M., Rockwell, D.L., 1998. The influence of subsurface moisture on rill system evolution. Earth Surface Processes and Landforms 23 (9), 773-789.
Burbank D.W., Leland, J., Fielding, E.J., Anderson, R.S., Brozovic, N., Reid, M.R., Duncan, C.C., 1996. Bedrock incision, rock uplift, and threshold hillslopes in the northwestern Himalayas. Nature 379 (6565), 505-510.
Byerlee, J., 1978. Friction of rock. Pure and Applied Geophysics 116, 615-626.
Cadell, H.M., 1888. Experimental researches in mountain building. Transactions of the Royal Society of Edinburgh 35, 337-357.
Carman, P.C., 1938. The determination of the specific surface of powders. Transactions of the Journal of the Society of Chemical Industry 57, 225-234.
Carman, P.C., 1956. Flow of Gases through Porous Media. Butterworths Scientific Publications, London. 169 pp.
Casagrande, A., 1932. Research on the Atterberg limits of soils. Public Roads 13 (8), 121-136.
Chamberlin, R.T., Miller, W.Z., 1918. Low-angle faulting. Journal of Geology 26 (1), 1-44.
Chapple, W.M., 1978. Mechanics of thin-skinned fold-and-thrust belts. Geological Society of America Bulletin 89 (8), 1189-1198.
Cobbold, P.R., Castro, L., 1999. Fluid pressure and effective stress in sandbox models. Tectonophysics 301 (1-2), 1-19.
Cobbold, P.R., Davy, P., Gapais, D., Rossello, E.A., Sadybakasov, E., Thomas, J.C., Tondji Biyo, J.J., Urreiztieta, M., 1993. Sedimentary basins and crustal thickening. Sedimentary Geology 86 (1-2), 7789.
Cobbold, P.R., Durand, S., Mourgues, R., 2001. Sandbox modelling of thrust wedges withfluid-assisted detachments. Tectonophysics 334 (3-4), 245-258.
Crave, A., Lague, D., Davy, P., Kermarrec, J.J., Sokoutis, D., Bodet, L., Compagnon, R., 2000. Analogue modelling of relief dynamics. Physics and Chemistry of the Earth A 25(6-7), 549-553.
Cruz, L., Teyssier, C., Perg, L., Take, A., Fayon, A., 2008. Deformation, exhumation, and topography of experimental doubly-vergent orogenic wedges subjected to asymmetric erosion. Journal of Structural Geology 30(1), 98-115.
Darcy, H., 1856. Les fontaines publiques de la ville de Dijon. Victor Dalmont, Paris. 647 pp.
Davis, D., Suppe, J., Dahlen, F.A., 1983. Mechanics of fold-and-thrust belts and accre-tionary wedges. Journal of Geophysical Research 88 (B12), 1153-1172.
Davy, P., Cobbold, P.R., 1991. Experiments on shortening of a 4-layer model of the continental lithosphere. Tectonophysics 188 (1-2), 1-25.
Ellis, S., Schreurs, G., Panien, P., 2004. Comparisons between analogue and numerical models of thrust wedge development. Journal of Structural Geology 26 (9), 1659-1675.
Flint, J.J., 1973. Experimental development of headward growth of channel networks. Geological Society of America Bulletin 84 (3), 1087-1094.
Gabbard, D.S., Huang, C., Norton, L.D., Steinhardt, G.C., 1998. Landscape position, surface hydraulic gradients and erosion processes. Earth Surface Processes and Land-forms 23 (1), 83-93.
Galland, O., Cobbold, P.R., Hallot, E., de Bremond d'Ars, J., Delavaud, G., 2006. Use of vegetable oil and silica powder for scale modelling of magmatic intrusion in a deforming brittle crust. Earth and Planetary Science Letters 243 (3-4), 786-804.
Graveleau, F., 2008. Interactions Tectonique, Erosion, Sedimentation dans les avant-pays de chafnes: modelisation analogique et etude des piemonts de l'est du Tian Shan (Asie Centrale). Universite Montpellier II, Montpellier. 487 pp.
Graveleau, F., Dominguez, S., 2008. Analogue modelling of the interactions between tectonics, erosion and

sedimentation in foreland thrust belts. Comptes Rendus Geoscience 340 (5), 324-333.
Graveleau, F., Dominguez, S., Malavieille, J., 2008. A new analogue modelling approach for studying interactions between surface processes and deformation in active mountain belt piedmonts. In: Corti, G. (Ed.), GeoMod 2008 Third International Geomodelling Conference. Bolletino di Geofisica teorica ed applicata, Villa la Pietra, Firenze, Italy, pp. 501-505.
Hack, J.T., 1957. Studies of longitudinal stream profiles in Virginia and Maryland. Unite States Geological Survey Professional Paper 294 (B), 45-97.
Halsey, T.C., Levine, A.J., 1998. How sandcastles fall. Physical Review Letters 80 (14), 3141-3144.
Hampel, A., Adam, J., Kukowski, N., 2004. Response of the tectonically erosive south Peruvian forearc to subduction of the Nazca Ridge: analysis of three-dimensional analogue experiments. Tectonics 23 (TC5003).
Hancock G.R., Willgoose, G.R., 2001. The interaction between hydrology and geomor-phology in a landscape simulator experiment. Hydrological Processes 15 (1), 115-133.
Hasbargen, L.E., Paola, C., 2000. Landscape instability in an experimental drainage basin. Geology 28 (12), 1067-1070.
Heller, P.L., Paola, C., Hwang, I., John, B., Steel, R., 2001. Geomorphology and sequence stratigraphy due to slow and rapid base-level changes in an experimental subsiding basin (XES 96-1). American Association of Petroleum Geologists Bulletin 85 (5),817-838.
Hornbaker, D.J., Albert, R., Albert, I., Barabasi, A.L., Schiffer, P., 1997. What keeps sandcastles standing ? Nature 387 (6635), 765.
Horsfield, W., 1977. An experimental approach to basement-controlled faulting. Geologie en Mijnbouw 56 (4), 363-370.
Hoth, S., Hoffmann-Rothe, A., Kukowski, N., 2007. Frontal accretion: an internal clock for bivergent wedge deformation and surface uplift. Journal of Geophysical Research 112, B06408. doi:10.1029/2006JB004357.
Howard, A.D., 1994. A detachment-limited model of drainage basin evolution. Water Resources Research 30 (7), 2261-2285.
Howard, A.D., Kerby, G., 1983. Channel changes in badlands. Geological Society of America Bulletin 94 (6), 739-752.
Howard, A.D., Dietrich, W.E., Seidl, M.A., 1994. Modeling fluvial erosion on regional to continental scales. Journal of Geophysical Research 99 (B7), 13971-13986.
Hubbert, M.K., 1951. Mechanical basis for certain familiar geologic structures. Bulletin of the Geological Society of America 62 (4), 355-372.
Jarvis, A., Reuter, H.I., Nelson, A., Guevara, E., 2008. Hole-filled seamless SRTM data V4. International Centre for Tropical Agriculture (CIAT).
Jordan, T.E., 1981. Thrust loads and foreland basin evolution, Cretaceous, western United States. American Association of Petroleum Geologists Bulletin 65 (12), 2506-2520.
Kirchner, J.W., Finkel, R.C., Riebe, C.S., Granger, D.E., Clayton, J.L., King, J.G., Megahan, W.F., 2001. Mountain erosion over 10 yr, 10 k.y., and 10 m.y timescales. Geology 29 (7), 591-594.
Konstantinovskaia, E., Malavieille, J., 2005. Erosion and exhumation in accretionary oro-gens: experimental and geological approaches. Geochemistry, Geophysics, Geosys-tems 6 (Q02006).
Konstantinovskaya, E., Malavieille, J., 2011. Thrust wedges with decollement levels and syntectonic erosion: a view from analogue models. Tectonophysics 502 (3-4),336-350.
Koss, J.E., Ethridge, F.G., Schumm, S.A., 1994. An experimental study of the effects of base-level change on fluvial, coastal plain and shelf systems. Journal of Sedimentary Research 64 (2b), 90-98.
Kozeny, J., 1927. Uber Kapillare Leitung des Wassers im Boden, Sitzungsber. Osterrei- chische Akademie der Wissenschaften 136 (2a), 271-306.
Krantz, R.W., 1991. Measurements of friction coefficients and cohesion for faulting and fault reactivation in laboratory models using sand and sand mixtures. Tectonophy- sics 188 (1-2), 203-207.
Lague, D., Crave, A., Davy, P., 2003. Laboratory experiments simulating the geomorphic response to tectonic uplift. Journal of Geophysical Research 108, B1. doi:10.1029/2002JB001785.
Lancien, P., Metivier, F., Lajeunesse, E., Cacas, M.C., 2005. Incision dynamics and shear stress measurements in submarine channels experiments. In: Parker, G., Garcia, M.H. (Eds.), 4th IAHR symposium on River, Coastal and Estuarine Morphody-namics. Taylor and Francis, pp. 527-533.
Landsat.org, a. Global Observatory for Ecosystem Services, Michigan State University http://landsat.org.
Larroque, C., Calassou, S., Malavieille, J., Chanier, F., 1995. Experimental modelling of forearc basin development during accretionary wedge growth. Basin Research 7 (3), 255-268.
Liu, Y., Metivier, F., Lajeunesse, E., Lancien, P., Narteau, C., Ye, B., Meunier, P., 2008. Measuring bedload in gravel-bed mountain rivers: averaging methods and sampling strategies. Geodinamica Acta 21 (1 -2), 81 -92.

Lohrmann, J., Kukowski, N., Adam, J., Oncken, O., 2003. The impact ofanalogue material properties on the geometry, kinematics, and dynamics of convergent sand wedges. Journal of Structural Geology 25 (10), 1691-1711.
Macedo, J., Marshak, S., 1999. Controls on the geometry of fold-thrust belt salients. Geological Society of America Bulletin 111 (12), 1808-1822.
Malavieille, J., 1984. Modelisation experimentale des chevauchements imbriques: application aux chaines de montagnes. Bulletin de la Societe Geologique de France 7 (1), 129-138.
Malavieille, J., 2010. Impact of erosion, sedimentation, and structural heritage on the structure and kinematics of orogenic wedges: analog models and case studies. GSA Today 20 (1),4-10.
Malavieille, J., Konstantinovskaya, E., 2010. Impact of surface processes on the growthof orogenic wedges: insights from analog models and case studies. Geotectonics 44(6), 541-558.
Malverti, L., Lajeunesse, E., Metivier, F., 2008. Small is beautiful: upscaling from micro-scale laminar to natural turbulent rivers. Journal of Geophysical Research 113, F04004. doi:10.1029/02007JF000974 002008.
Mandl, G., de Jong, L.N.J., Maltha, A., 1977. Shear zones in granular material: an experimental study of their structure and mechanical genesis. Rock Mechanics and Rock Engi-neering9 (2-3), 95-144.
Metivier, F., Meunier, P., 2003. Input and output flux correlations in an experimental braided stream: implications on the dynamics of bed load transport. Journal of Hydrology 271 (1-4), 22-38.
Metivier, F., Lajeunesse, E., Cacas, M.C., 2005. Submarine canyons in the bathtub. Journal ofSedimentary Research 75 (1), 6-11.
Mitarai, N., Nori, F., 2006. Wet granular materials. Advances in Physics 55 (1 -2), 1 -45.
Molnar, P., Lyon-Caen, H., 1988. Some simplephysicalaspects ofthesupport, structure and Evolution of Moun tain belts. GeologicalSocietyofAmericaSpecialPaper218,179-207.
Montgomery, D.R., Brandon, M.T., 2002. Topographic controls on erosion rates in tec-tonically active mountain ranges. Earth and Planetary Science Letters 201 (3-4),481-489.
Mount, J.F., 1995. California Rivers and Streams: The Conflict between Fluvial Process and Land Use. University of California Press, Berkeley, California. 359 pp.
Mourgues, R., Cobbold, P.R., 2003. Some tectonic consequences of fluid overpressures and seepage forces as demonstrated by sandbox modelling. Tectonophysics 376 (1-2), 75-97.
Mourgues, R., Cobbold, P.R., 2006. Thrust wedges and fluid overpressures: sandbox models involving pore fluids. Journal of Geophysical Research 111, B05404.doi:10.1029/2004JB003441.
Mulugeta, G., Koyi, H., 1987. Three-dimensional geometry and kinematics of experimental piggyback thrusting. Geology 15 (11), 1052-1056.
Niemann, J.D., Hasbargen, L.E., 2005. Acomparison ofexperimental and naturaldrainage basin morphology across a range of scales. Journal of Geophysical Research 110, F04017. doi:10.1029/2004JF000204.
Ori, G.G., Friend, P.F., 1984. Sedimentary basins formed and carried piggyback on active thrust sheets. Geology 12 (8), 475-478.
Panien, M., Schreurs, G., Pfiffner, AO., 2006. Mechanical behaviour of granular materials, used in analogue modelling: insights from grain characterisation, ring-shear tests and analogue experiments. Journal of Structural Geology 28 (9), 1710-1724.
Paola, C., Mullin, J., Ellis, C., Mohrig, D., Swenson, J.B., Parker, G., Hickson, T., Heller, P.L., Pratson, L., Syvitski, J., Sheets, B., Strong, N., 2001. Experimental stratigraphy. GSA Today 11,4-9.
Paola, C., Straub, K., Mohrig, D., Reinhardt, L., 2009. The "unreasonable effectiveness" of stratigraphic and geomorphic experiments. Earth-Science Reviews 97 (1-4), 1-43.
Peakall,J., Ashworth, P.J., Best, J.L., 1996. Physical modelling in fluvial geomorphology: principles, applications and unresolved issues. In: Rhoads, B.L., Thorn, C.E. (Eds.), The Scientific Nature of Geomorphology. Wiley & Sons, Chichester, pp. 221-253.
Pelletier, J.D., 2003. Drainage basin evolution in the Rainfall Erosion Facility: dependence on initial conditions. Geomorphology 53 (1-2), 183-196.
Phillips, L.F., Schumm, S.A., 1987. Effect of regional slope on drainage networks. Geology 15 (9), 813-816.
Pierrat, P., Caram, H.S., 1997. Tensile strength of wet granular materials. Powder Technology 91 (2), 83-93.
Pierrat, P., Agrawal, D.K., Caram, H.S., 1998. Effect of moisture on the yield locus ofgranular materials: theory of shift. Powder Technology 99 (3), 220-227.
Pinet, P., Souriau, M., 1988. Continental erosion and large-scale relief. Tectonics 7 (3),563-582.
Poisson, B., 2002. Impact du climat et de la tectonique sur revolution geomorphologique d'un piemont: Exemple du piemont Nord du Tian Shan depuis la fin du Pleistocene. Universite de Paris XI, Paris. 260 pp.
Ramberg, H., 1981. Gravity, Deformation and the Earth's Crust, London. 452 pp.
Reigber, C., Michel, G.W., Galas, R., Angermann, D., Klotz, J., Chen, J.Y., Papschev, A., Arslanov, R., Tzurkov, V.E., Ishanov, M.C., 2001. New space geodetic constraints on the distribution of deformation in Central Asia. Earth and Planetary Science Letters 191 (1), 157-165.

Reuter, H.I., Nelson, A., Jarvis, A., 2007. An evaluation of void filling interpolation methods for SRTM data. International Journal of Geographic Information Science 21 (9), 983-1008.
Richefeu, V., El Youssoufi, M.S., Radja'i, F., 2006. Shear strength properties of wet granular materials. Physical Review E 73, 051304.
Richefeu, V., El Youssoufi, M.S., Peyroux, R., Radja'i, FA, 2007. A model of capillary cohesion for numerical simulations of 3D polydisperse granular media. International Journal for Numerical and Analytical Methods in Geomechanics 32 (11), 1365-1383.
Rieke-Zapp, D.H., Nearing, M.A., 2005. Slope shape effects on erosion: a laboratory study. Soil Science Society of America Journal 69 (5), 1463-1471.
Rigon, R., Rodriguez Iturbe, I., Maritan, A., Giacometti, A., Tarboton, D., Rinaldo, A., 1996. On Hack's law. Water Resources Research 32 (11), 3367-3374.
Rohais, S., 2007. Architecture stratigraphique et flux sedimentaires sur la marge sud du golfe de Corinthe (Grece): Analyse de terrain, modelisations experimentales et numeriques. Universite de Rennes, Rennes. 386 pp.
Rohais, S., Bonnet, S., Eschard, R., 2011. Sedimentary record of tectonic and climatic erosional perturbations in an experimental coupled catchment-fan system. Basin Research 23,1-15.
Rossi, D., Storti, F., 2003. New artificial granular materials for analogue laboratory experiments: aluminium and siliceous microspheres. Journal of Structural Geology 25 (11), 1893-1899.
Rumpf, H.R., 1962. The strength of granules and agglomerates. In: Knepper, W.A. (Ed.), Agglomeration. Wiley, New York, pp. 379-418.
Salles, C., Poesen, J., Sempere-Torres, D., 2000. Kinetic energy of rain and its functional relation with intensity. Journal of Hydrology 257 (1-4), 256-270.
Schellart, W.P., 2000. Shear test results for cohesion and friction coefficients for different granular materials: scaling implications for their usage in analogue modelling. Tectonophysics 324 (1-2), 1-16.
Schubert, H., 1984. Capillary forces-modeling and application in particulate technology. Powder Technology 37 (1), 105-116.
Schulze, D., 1994. Entwicklung und anwendung eines neuartigen Ringshergerates. Auf-bereitungstechnik 35 (10), 524-535.
Schumm, S.A., Parker, R.S., 1973. Implications of complex response of drainage systems for quaternary alluvial stratigraphy. Nature Physical Sciences 243 (128), 99-100.
Schumm, S.A., Rea, D.K., 1995. Sediment yield from disturbed earth systems. Geology 23 (5), 391-394.
Schumm, S.A., Mosley, M.P., Weaver, W.E., 1987. Experimental Fluvial Geomorphology. John Wiley, New York. 413 pp.
Shepherd, R.G., Schumm, S.A., 1974. Experimental study of river incision. Geological Society of America Bulletin 85 (2), 257-268.
Snyder, N.P., Whipple, K.X., Tucker, G.E., Merritts, D.J., 2000. Landscape response to tectonic forcing: DEM elevation model analysis of stream profiles in the Mendocino Triple Junction Region, Northern California. Geological Society of America Bulletin 112 (8), 1250-1263.
Soulie, F., El Youssoufi, M.S., Cherblanc, F., Saix, C., 2006. Capillary cohesion and mechanical strength of polydisperse granular materials. The European Physical Journal E: Soft Matter and Biological Physics 21 (4), 349-357.
Stock, J.D., Montgomery, D.R., 1999. Geologic constraints on bedrock river incision using the stream power law. Journal of Geophysical Research 104 (B3),4983-4993.
Storti, F., Salvini, F., McClay, K., 2000. Synchronous and velocity-partitioned thrusting and thrust polarity reversal in experimentally produced, doubly-vergent thrust wedges: implications for natural orogens. Tectonics 19 (2), 378-396.
Strahler, A.N., 1957. Quantitative analysis of watershed geomorphology. American Geophysical Union Transactions 38, 913-920.
Strak, V., Dominguez, S., Petit, C., Meyer, B., Loget, N., 2011. Interaction between normal fault slip and erosion on relief evolution: insights from experimental modelling. Tectonophysics 513 (1-4), 1-9.
Summerfield, M.A., Hulton, N.J., 1994. Natural controls of fluvial denudation rates in major world drainage basins. Journal of Geophysical Research 99 (B7),13871-13883.
Suppe, J., 1981. Mechanics of mountain building and metamorphism in Taiwan. Memoir of the Geological Society of China 4,67-89.
Tarboton, D.G., Bras, R.L., Rodriguez-Iturbe, I., 1989. Scaling and elevation in river networks. Water Resources Research 25 (9), 2037-2051.
Tucker, G.E., Whipple, K.X., 2002. Topographic outcomes predicted by stream erosion models: sensitivity analysis and intermodel comparison. Journal of Geophysical Research 107 (B9), 2179.
Turowski, J.M., Lague, D., Crave, A., Hovius, N., 2006. Experimental channel response to tectonic uplift. Journal of Geophysical Research 111 (F03008).

Van Mechelen, J.L.M., 2004. Strength of moist sand controlled by surface tension for tectonic analogue modelling. Tectonophysics 384 (1-4), 275-284.
Wang, W.H., Davis, D.M., 1996. Sandbox model simulation of forearc evolution and noncritical wedges. Journal of Geophysical Research 101 (B5), 11329-11340.
Weijermars, R., Schmeling, H., 1986. Scaling of Newtonian and non-Newtonian fluid dynamics without inertia for quantitative modelling of rock flow due to gravity. Physics of the Earth and Planetary Interiors 43 (4), 316-330.
Wessel, P., Smith, W.H.F., 1991. Free software helps map and display data. In: AGU (Editor), EOS Transaction 72, pp. 445-446.
Whipple, K.X., Tucker, G.E., 1999. Dynamics of the stream power river incision model: Implications for height limits of mountain ranges, landscape response timescales and research needs. Journal of Geophysical Research 104 (B8), 17661-17674.
Wilkerson, M.S., Marshak, S., Bosworth, W., 1992. Computerized tomographic analysis of displacement trajectories and three-dimensional fold geometry above oblique thrust ramps. Geology 20 (5), 439-442.
Wittmann, R., Kautzky, T., Hiibler, A., Liischer, E., 1991. A simple experiment for the examination of dendritic river systems. Die